

1 **Spatiotemporal Drivers of Hydrochemical Variability in a**
2 **Tropical Glacierized Watershed in the Andes**

3 **Leila Saberi¹, G.-H. Crystal Ng^{1,2}, Leah Nelson¹, Wei Zhi³, Li Li³, Jeff La Freniere⁴,**
4 **Morgan Johnstone¹**

5 ¹Department of Earth Sciences, University of Minnesota – Twin Cities, Minneapolis, MN 55455, USA

6 ²Saint Anthony Falls Laboratory, University of Minnesota – Twin Cities, Minneapolis, MN 55414, USA

7 ³Department of Civil & Environmental Engineering, Pennsylvania State University, University Park, PA 16802-1294, USA

8 ⁴Department of Geography, Gustavus Adolphus College, St. Peter, MN 56082, USA

9 **Key Points:**

- 10 · Model calibration to hydrochemical data improves constraints on subsurface flowpaths
11 and fluxes.
- 12 · Mineral dissolution controls mean solute quantities in the watershed, while evapotran-
13 spiration controls spatial and seasonal variability.
- 14 · Glacial meltwater enhances ion export via greater dissolution and flushing from sub-
15 surface.

Corresponding author: Leila Saberi, saber017@umn.edu

Abstract

Little is currently known about the hydrochemistry of tropical glacierized mountain watersheds, which are among the most vulnerable systems in the world. Glacier retreat may impact their export of nutrients, with possible implications for downstream ecosystems. Solute export depends on dynamic and heterogeneous processes within the watershed, which calls for investigations of the different factors controlling hydrochemical variability. To examine these in a sub-humid glacierized watershed in Ecuador, we implemented a hydrological model that incorporates reactive transport, RT-Flux-PIHM. Our results demonstrate that calibrating the model to hydrochemical in addition to hydrological data is important for constraining groundwater fluxes, which we found to contribute 78% of stream discharge and to include 35% of the total glacial meltwater. Stream chemistry fluctuations are strongly controlled by varying contributions of groundwater, which contains high concentrations of reactive ions predominantly sourced from silicate mineral dissolution. The spatial variability in these concentrations, however, is driven more by heterogeneous evapotranspiration resulting from sharp montane vegetation gradients. With this concentrating effect, evapotranspiration also largely determines seasonal patterns in groundwater chemistry, with highest concentrations occurring in dry seasons, even when dissolution rates are low due to low soil moisture. While groundwater serves as a primary end-member source of streamwater, glacier melt-dominated surface runoff acts as a second source that imposes dilution events on an otherwise chemostatic concentration and discharge (C-Q) graph. Glacier melt overall decreases stream concentrations and increases discharge, with the latter effect dominating such that solute exports (C^*Q) increase by 23% with melt.

1 Introduction

Glacial meltwater in mountainous watersheds is an important source of water for communities living below them (Messerli et al., 2004; Kaser et al., 2010). Rising temperatures due to global warming results in increased rates of glacier retreat, raising concerns for regional water resource availability (Mark et al., 2017; Barnett et al., 2005). Growing evidence has shown that the rate of warming is highest in low latitudes and high altitudes. This includes tropical glacierized watersheds, more than 99% of which reside in the Andes (Bradley, 2006; Pepin et al., 2015). Tropical glacierized watersheds already experience year-round melt under present conditions (Kaser & Osmaston, 2002), and thus, they are highly vulnerable to on-going climate change and can be used as an early-indicator of climate change impacts on glacierized watersheds worldwide.

Much attention has been directed to the impact of glacier retreat in the Andes on streamflow (Barnett et al., 2005; Ostheimer et al., 2005; Bradley, 2006; Mark & McKenzie, 2007; IPCC, 2007; Baraer et al., 2009; Saberi et al., 2019; Somers et al., 2019). In contrast, little attention has been paid to the potential hydrochemical impacts of glacier retreat. This represents a critical knowledge gap, because many tropical glacierized watersheds in the Andes likely undergo high weathering rates and serve as important sources of solutes to the Amazon basin. The majority of Andean glacierized mountains are located within the Andean volcanic belt (Stern, 2004) and are mainly composed of highly reactive silicate minerals (Stallard & Edmond, 1983; Ugolini et al., 2002; Torres et al., 2015). The weathering of silicate minerals increases significantly with high temperature and high moisture (Ugolini et al., 2002; White et al., 1998), conditions commonly found in humid tropical climates. Further, the weathering yield of minerals from combined physical and chemical processes has been noted worldwide to be greater in glacierized watersheds compared to non-glaciated catchments (Torres et al., 2017). While some weathered products form secondary minerals, most of them move into streams and are transported downgradient (Milner et al., 2017). Even though Andean glacierized mountains are located thousands of kilometers away from the Amazon river estuary and constitute only 13% of the Amazon basin, they are believed to be the main source of solutes that support ecological productivity in the basin, including sodium (Na^+), calcium (Ca^{2+}), and magnesium (Mg^{2+}) (Gibbs, 1967; McClain & Naiman, 2008). However, this linkage between the Andes and Amazon may be threatened by environmental changes, and this impact on the Amazon Basin's ecological productivity is not well-understood. This calls for investigations into the hydrogeochemical function of tropical glacierized watersheds in order to understand their response to climate change and the corresponding ecological impacts.

Controls on the hydrochemistry of glacierized mountainous watersheds have been well-studied in

69 temperate climates; these include meteorological drivers, geology, topography, and land-cover over
70 different spatial and temporal scales (Devito et al., 2005; Williams et al., 2015; Engel et al., 2019).
71 Meteorological conditions in particular have been found to have a significant influence on hydro-
72 chemical variability by increasing melt rates in temperate conditions (Milner et al., 2017). Temper-
73 ature and radiation are the main driving forces for snow and ice melt (Sicart et al., 2008). Some
74 previous studies in temperate glacierized watersheds found that solute concentrations are lower dur-
75 ing high melt seasons due to the discharge of dilute meltwater into streams (Brown, 2002; Hindshaw
76 et al., 2011; Kumar et al., 2019; Engel et al., 2019). However, other studies found that in-stream
77 silica (SiO_2) [Anderson et al., 2005] and other major ion concentrations (Lewis et al., 2012; Stachnik
78 et al., 2016) increase during high melt seasons mainly due to the increase in the hydrological connect-
79 tivity of the catchment, which accelerates mineral dissolution. Bedrock and surficial geology also
80 play an important role in controlling watershed hydrochemistry, both directly through geochemical
81 input or immobilization of solutes (Tranter et al., 1996; Katsuyama et al., 2010) as well as indirectly
82 through their physical influence on flow pathways (Farvolden, 1963; McGuire et al., 2005; Tetzlaff
83 et al., 2009; Maher, 2011; Benettin et al., 2015).

84 Compared to temperate mountainous watersheds (Collins, 1999; Feng et al., 2012; Milner et al.,
85 2009; Brighenti et al., 2019), relatively little is known about the factors controlling stream chem-
86 istry in tropical glacierized mountainous systems. Hydrochemical observations have mostly been
87 used only as conservative tracers to determine relative meltwater contributions to stream discharge
88 (Mark & McKenzie, 2007; Baraer et al., 2009, 2015; Wilson et al., 2016; Minaya, 2016; Saberi et
89 al., 2019). However, some recent studies have revealed dynamic and complex hydrochemical pro-
90 cesses. Fortner et al. (2011) showed that glacier retreat in the Peruvian Cordillera Blanca is exposing
91 sulfide-rich rock outcrops, leading to impaired water quality in streams. A set of hydrochemical stud-
92 ies spanning the Andes to Amazon transition included non-glacierized watersheds in the Peruvian
93 Andes and showed that spatial heterogeneity among sub-catchments control temporal variations in
94 stream discharge chemistry through dilution or weathering effects (Torres et al., 2015, 2017; Baronas
95 et al., 2017). Together, these initial hydrochemical investigations in the tropical Andes point to the
96 importance of understanding the role of spatiotemporal variability in driving the export of solutes.

97 Regardless of climate, many hydrochemical studies rely on stream concentration and discharge (C-
98 Q) relationship analysis (Godsey et al., 2009). An advantage to this approach is its relative ease of
99 implementation with a single surficial measurement point at the stream outlet. C-Q relationship anal-
100 ysis serves as an indirect way of inferring processes within the watershed that give rise to observed
101 changes in concentration and discharge. However, because of the lack of explicit, fine-scale process
102 examination in C-Q analysis, uncertainties persist when evaluating the individual roles of different
103 hydrological and hydrochemical processes (Li et al., 2017). In particular, limitations in C-Q analysis
104 for evaluating groundwater processes present a major weakness in many snow and ice-covered moun-
105 tainous watersheds, because various hydrological studies have shown that in addition to melt runoff,
106 groundwater can also contribute significantly to streamflow (Huth et al., 2004; Hood et al., 2006;
107 Tague et al., 2008; Baraer et al., 2015; Andermann et al., 2012; Pohl et al., 2015; Engel et al., 2016;
108 Harrington et al., 2018; Saberi et al., 2019; Somers et al., 2019). Some studies in non-glacierized
109 tropical Andean watersheds have tackled the challenge of spatially lumped C-Q analysis by evalu-
110 ating the sub-catchment C-Q relationships to show that varying sub-tributary discharge controls
111 conditions at the outlet (Torres et al., 2015; Baronas et al., 2017). This approach nonetheless only
112 looks explicitly at surface processes at different sub-catchments and can only offer indirect evidence
113 for subsurface weathering and geochemical reactions (Torres et al., 2015; Baronas et al., 2017); in
114 fact, the authors acknowledge that quantitative assessment of fluid transit and mineral contact times
115 in the ground are precluded by data sparsity in the remote Andean sites (Torres et al., 2015).

116 A recently developed, spatially distributed and physically based model that integrates watershed hy-
117 drology and reactive transport, "RT-Flux-PIHM (Bao et al., 2017)", is now making it possible to di-
118 rectly evaluate spatiotemporal controls on the hydrochemistry within a watershed without exhaustive
119 measurements (Li et al., 2017; Zhi et al., 2019). Previous applications of the model at two intensive
120 study watersheds in the temperate U.S. (Susquehanna Shale Hills Critical Zone Observatory and
121 Coal Creek in Crested Butte, CO) included an explicit representation of subsurface hydrochemistry,
122 which led to quantitative insights into drivers of the degree of chemostasis in the watersheds. Re-
123 sults show strong seasonal controls through both hydrologic (effects of connectivity, solute flushing,

124 and subsurface flow contributions) and geochemical (effect of mineral reactivity via wetted surfaces
 125 and dissolved organic carbon reactions) processes across the entire watershed (Li et al., 2017; Zhi
 126 et al., 2019; Wen et al., 2020). These early applications are paving the way for new questions, such
 127 as how other types of seasonal patterns (e.g., warmer and wetter tropical conditions with additional
 128 snow and ice melt contributions), lithologies (e.g., silicate-dominated volcanic soils underlain by
 129 fractured bedrock), and vegetation coverage (e.g., discrete vegetation line in high mountain water-
 130 sheds) might support or counteract the tendency for chemostasis. In the tropical Andes, the degree of
 131 chemostasis and corresponding variations in nutrient export have important implications for critical
 132 downstream ecosystems as glaciers retreat.

133 In this study, we leverage RT-Flux-PIHM to answer two main questions in a sparsely instrumented
 134 glacierized watershed on Volcán Chimborazo in the tropical Ecuadorian Andes: (1) What is the role
 135 of hydrological and geochemical processes in controlling the spatiotemporal variability of concen-
 136 trations of major ions in groundwater and streamwater? (2) What is the influence of glacial melt
 137 on hydrochemical variability in the watershed? The answer to the first question will provide gen-
 138 eral insights into vulnerable glacierized watersheds. Because we hypothesize that the influence of
 139 glacial melt will depend on its interactions with hydrogeological, ecohydrological, and weathering
 140 processes across the watershed, the answer to the first question will also help to address the second
 141 question.

142 2 Study Site Description

143 Volcán Chimborazo is a glacierized stratovolcano in Ecuador (Figure 1) that supplies water to
 144 over 200,000 people (INEC, 2010). Chimborazo experiences an inner tropical climate, characterized
 145 by minimal annual temperature variation ($\sim 2^\circ\text{C}$ variability) and moderately seasonal precipitation
 146 with generally two wetter seasons (February-May and October-November) and two drier seasons
 147 that have less amounts of precipitation (Clapperton, 1990). Because of the Amazon Basin to the east
 148 (Vuille & Keimig, 2004; Smith et al., 2008), more humid conditions can be found on the northeast
 149 flank with more precipitation (2000 mm/yr) than the southwest (500 mm/yr) (Clapperton, 1990). El
 150 Niño and La Niña events cause variability in temperature and precipitation, with El Niño generally
 151 bringing drier and hotter conditions and La Niña wetter and cooler conditions throughout the An-
 152 des (Vuille & Bradley, 2000; Bradley et al., 2003; Wagnon et al., 2001; Francou, 2004; Vuille &
 153 Keimig, 2004; Smith et al., 2008). El Niño events have been found to potentially enhance glacier
 154 ablation (Francou, 2004; Favier, 2004; Vuille et al., 2008; Veettil et al., 2014). Within the June
 155 2016-June 2017 time frame of this study, a strong El Niño event brought higher temperature and
 156 lower precipitation than normal to the watershed during November to February. Also during this
 157 year, wet conditions were observed over June to October (2015) and March to May (2016), which
 158 differ slightly from the general wet months noted above.

159 Temperatures have increased by $0.11^\circ\text{C}/\text{decade}$ around Volcán Chimborazo since 1986 (Vuille et
 160 al., 2008; La Frenierre & Mark, 2017), which has been partly responsible for a 21% reduction in
 161 ice surface area from 1986-2013 and 180 m increase in the mean minimum elevation of clean ice
 162 (La Frenierre & Mark, 2017). Though instrumental data are ambiguous, community members in-
 163 dicate the local precipitation has decreased in recent decades (La Frenierre & Mark, 2017). This
 164 study focuses on the 7.5 km² Gavilan Machay sub-catchment on the sub-humid northeast flank of
 165 Chimborazo (Figure 1). Gavilan Machay has an altitude range of 3800 to 6400 m a.s.l and is 34%
 166 glacierized by the Reschreiter Glacier. Water from Gavilan Machay eventually reaches the Amazon
 167 below the confluence of Río Marañon, the principal upper tributary of the Amazon River, via the
 168 Río Mocha, Río Ambato, Río Chambo, and Río Pastaza. Gavilan Machay is of particular concern
 169 because it discharges into the Río Mocha channel immediately upstream of the Boca Toma diversion
 170 point (3895 m a.s.l. elevation) for the largest irrigation system on Volcán Chimborazo. Saberi et al.
 171 (2019) found that currently stream discharge from Gavilan Machay may contain up to 50% glacier
 172 meltwater, which has future implications for the downstream irrigation system as the glaciers con-
 173 tinue to retreat.

174 Páramos – the biologically rich grasslands of the tropical Andes– are the most common ecosystem
 175 across the watershed below about 4600 m a.s.l. (Figure 2a). Ecologically, the páramo has high plant
 176 diversity (>5000 species), mainly consisting of tussock grasses, cushion plants, dwarf shrubs, ground

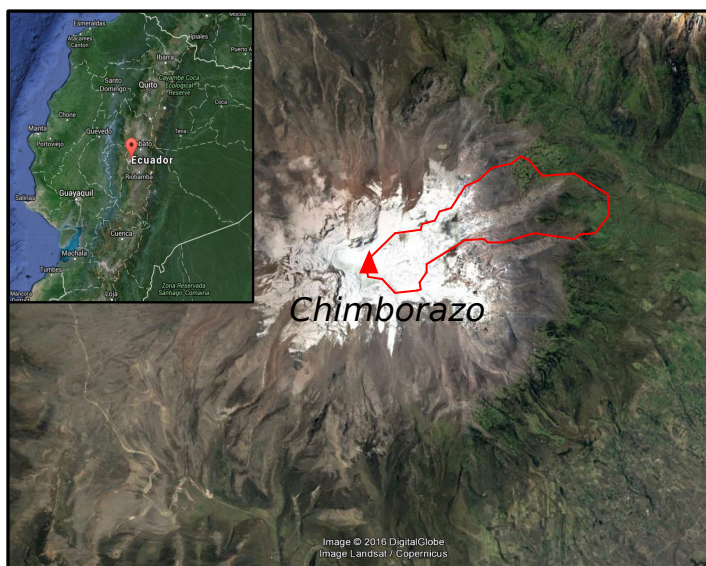


Figure 1: Satellite image of Volcán Chimborazo with the Gavilan Machay watershed outlined in red and its location in Ecuador shown in the inset map.

177 rosettes, and giant rosettes. Wet páramos are mainly composed of Andosol soils of volcanic origin
 178 and have high porosity and water retention capacity (Podwojewski et al., 2002; Buytaert et al., 2006;
 179 Buytaert & Beven, 2011; Minaya, 2016). The primary geology of Chimborazo consists of layered
 180 lava and pyroclastic flows, overlaid by thick ash deposits and vitric andosol (Figure 2b) (Barba et
 181 al., 2008; Samaniego et al., 2012). The morphology of the watershed has been influenced largely by
 182 glacial deposits and moraines from the Last Glacial maximum (LGM: 33-14 ka), the Late Glacial
 183 (LG: 13-15 ka), and the Neo-Glacial Period (NG: <5 ka). The presence of young volcanic fractured
 184 bedrock along with páramo soils and glacial deposits (Barba et al., 2005; Samaniego et al., 2012)
 185 facilitates water movement through the subsurface, which enhances both groundwater contribution
 186 to streamflow and weathering processes that release ions into the water (Stallard & Edmond, 1983).
 187 Previous hydrochemical observations in the Gavilan Machay watershed shows that the total dissolved
 188 solids concentrations in springs, proxies for groundwater, and streamflow increases as the elevation
 189 decreases (Saberí et al., 2019). This suggests that mineral reactions are releasing solutes into water
 190 as it flows downgradient in the watershed. Based on observations, sodium, calcium, and magnesium
 191 are the major ions present in the groundwater and surface water.

192 3 Geochemical Observations

193 3.1 Sites and Sampling Method

194 Three locations were selected for soil sampling along an elevation gradient (at 4510, 4240, and
 195 3990 m a.s.l.) (Figure 2b). The highest elevation sample (S-1) was collected from moraine sediments,
 196 while the other two (S-2 and S-3) were taken near the stream channel (Figure 2b). A 3-inch diameter
 197 auger was used for soil profile sampling. At all sampling sites, shallow refusal was hit on buried
 198 cobbles and a single sample was collected from 3 and 5 cm depth. Two rock samples were collected
 199 at exposed outcrops, at 4950 m a.s.l. and 4000 m a.s.l. (R-1 and R-2, respectively, Figure 2b). The
 200 high elevation rock sample (R-1) was collected from Guano lava flows while the low elevation rock
 201 sample was collected from Holocene pyroclastic flow deposits (Barba et al., 2008). Details about
 202 the water sampling (locations in figure 2a) and analysis are in Saberí et al. (2019). Samples taken at
 203 spring sites were used to represent groundwater and will be referred to as "groundwater" to simplify
 204 the text.

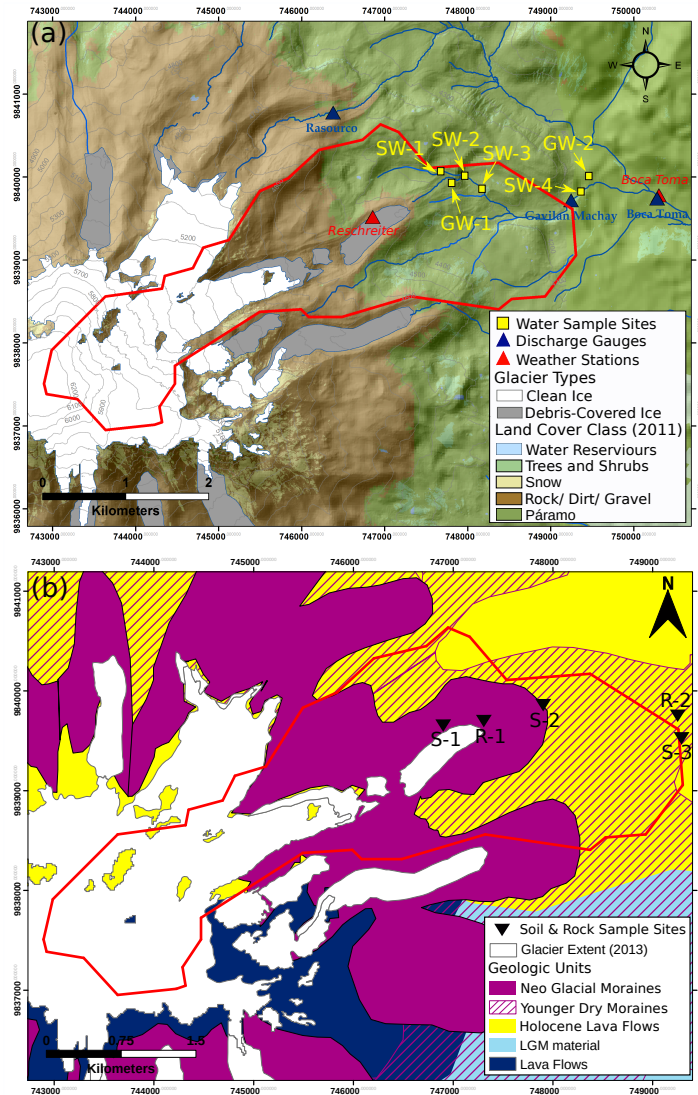


Figure 2: (a) Land cover and locations of monitoring stations and water sampling within the Gavilan Machay watershed. (b) Geologic map of Volcán Chimborazo and locations of soil and rock sampling within the Gavilan Machay watershed. The boundary of the Gavilan Machay watershed is outlined in red. Maps were adapted from McLaughlin (2017).

205 3.2 XRD Analysis and Results

206 Soil samples were air-dried and stored in resealable bags. Bulk soil and rock composition was
 207 determined using X-ray diffraction (XRD) analysis. Aggregate soils and rock were hand-ground to a
 208 fine powder. To separate the fine fraction from the aggregate sample, approximately 50g of each bulk
 209 soil sample was dry-sieved by hand. Organic matter was removed from the samples by the addition
 210 of a 3% hydrogen peroxide (H_2O_2) solution following Poppe et al. (2001) (USGS Open-File Report
 211 01-041). Minerals in the bulk rock and soil samples were identified using XRD analysis. Samples
 212 were mounted on a glass slide using a smear technique to achieve random orientation. A Rigaku
 213 MiniFlex300 X-ray diffractometer was used to scan the samples from 5° to 65° 2θ at 30 kV voltage
 214 and 10mA current with Cr- $K\alpha$ radiation. XRD patterns were analysed using the Jade software ver-
 215 sion 7.5.

Results from the XRD analysis indicate that the Gavilan Machay watershed is predominantly composed of aluminosilicate minerals including feldspar, pyroxene, and amphibole, which is consistent with most andosols worldwide (Shoji et al., 1994). Although the humid conditions in Gavilan Machay would generally be expected to promote high rates of chemical weathering, possibly producing clay minerals, the XRD results show no crystalline-clay minerals. Through grain size analysis, however, we found 8.5% and 18% of the bulk samples collected from 0-30 cm depth at 3800 m a.s.l. and 4500 m a.s.l., respectively, were clay- and silt-sized particles (smaller than 63 μm diameter). These estimates are consistent with previous soil studies on Chimborazo. Podwojewski et al. (2002) showed that shallow soil samples at 3800-4200 m a.s.l. on the drier northwestern flank of Chimborazo contain an average of 8.5% clay. Bartoli et al. (2007) found a slightly higher amount of 23% organo-mineral clay at 3800 m a.s.l. using a larger 2 mm diameter definition. It is likely the fine-grain fraction in our samples also contains organo-mineral clays that were resistant to our hydrogen peroxide treatment, as well as minerals with poor crystalline structure. Bartoli et al. (2007) characterized the Chimborazo's soils as aluandic andosols, which are regarded as non-allophanic andosol predominantly composed of aluminum complexed with organic matter (Takahashi & Shoji, 2002). The XRD analysis indicates that the bulk soil mineralogy is primarily dominated by that of the parent bedrock. As shown in Table 1, soil sample S-1 resembles the nearby rock sample R-1 (see map in Figure 2b) with three minerals in common from the feldspar and pyroxene mineral classes. Soil sample S-2 resembles rock sample R-2 based on similar feldspar minerals and proximity; soil sample S-3 likely originates from the R-2 rock sample, sharing minerals from both feldspar and pyroxene classes. Minerals from the amphibole class were present only in the R-1 rock sample and not in any soil samples, which suggests that they are relatively resistant to weathering compared to other classes. Even though the soil and rock properties have some differences, they are comprised of similar classes of minerals (feldspar and pyroxene) throughout the watershed. Relatively homogeneous soil characteristics have been observed elsewhere in the páramos of the Ecuadorian Andes, probably due to similar parent sources throughout an area (Buytaert et al., 2006). Different climatic conditions, however, can result in slight differences in soil properties (Buytaert et al., 2006; Podwojewski et al., 2002). Our findings indicate that the underlying bedrock geology is the major controller of soil mineralogy in the watershed, suggesting that the surficial sediment and deeper bedrock aquifers in the watershed may share similar hydrochemical signatures.

	Mineral	Chemical Formula	R-1	S-1	R-2	S-2	S-3
Feldspar	Albite	$\text{Na}(\text{AlSi}_3\text{O}_8)$			✓	✓	✓
	Anorthite	$\text{Ca}(\text{Al}_2\text{Si}_2\text{O}_8)$	✓	✓	✓		✓
	Andesine	$\text{Na}_{0.685}\text{Ca}_{0.347}\text{Al}_{1.46}\text{Si}_{2.54}\text{O}_8$	✓	✓			
	Labradorite	$\text{Na}_{0.45}\text{Ca}_{0.55}\text{Al}_{1.5}\text{Si}_{2.5}\text{O}_8$		✓			
	Sanidine	$\text{K}(\text{Si}_3\text{Al})\text{O}_8$	✓				✓
	Anorthoclase	$(\text{Na}_{0.75}\text{K}_{0.25})(\text{AlSi}_3\text{O}_8)$	✓		✓	✓	✓
Pyroxene	Enstatite ferroan	$\text{Mg}_{1.1}\text{Fe}_{0.87}\text{Ca}_{0.03}\text{Si}_2\text{O}_6$	✓	✓	✓		
	Diopside	$\text{Ca}(\text{Mg},\text{Al})(\text{Si},\text{Al})_2\text{O}_6$	✓		✓		✓
Amphibole	Arfvedsonite	$\text{Na}_3(\text{Fe},\text{Mg})_4\text{FeSi}_8\text{O}_{22}(\text{F},\text{OH})_2$	✓				
	Actinolite	$(\text{Fe},\text{Mg},\text{Ca},\text{Na},\text{Mn})_7(\text{Si},\text{Al})_8\text{O}_{22}(\text{OH})_{1.9}$	✓				

Table 1: Soil Mineralogy of Volcán Chimborazo. S-1, S-2, and S-3 are soil samples. R-1 and R-2 are rock samples from outcrops in the watershed. Sample locations are shown in Figure 2.

4 Model Description

4.1 RT-Flux-PIHM

Spatially distributed watershed models can integrate surface hydrology and groundwater flow through time and space to allow for the evaluation of their joint control on streamflow. Flux-PIHM (Shi et al., 2013) integrates land-surface and hydrologic simulations through a combination of two modules, the Noah land surface model (Noah-LSM) (Ek et al., 2003) and the PIHM hydrological

253 model (Qu & Duffy, 2007). The multicomponent reactive transport module RT is an add-on to
 254 Flux-PIHM (Bao et al., 2017). The RT module takes calculated water fluxes and storage from Flux-
 255 PIHM (i.e. surface runoff, channel routing, infiltration, recharge, and subsurface lateral flow) and
 256 simulates hydrochemical processes including solute transport (advection, dispersion, and diffusion)
 257 and chemical reactions and outputs aqueous and solid phase geochemical concentrations. In addition
 258 to surface and subsurface water flow, evapotranspiration (ET) is simulated in the model as another
 259 key hydrologic flux that has a non-geochemical influence on solute concentrations. RT can simulate
 260 both equilibrium-controlled reactions including aqueous complexation, ion exchange, and surface
 261 complexation, and kinetically controlled reactions including mineral dissolution, precipitation, and
 262 redox reactions (Bao et al., 2017). Reactive transport is modeled in both the unsaturated and saturated
 263 zones. It is assumed that the surface runoff water has a very short interaction time with minerals and
 264 is not considered to undergo geochemical reactions in the RT module.

265 The rate of kinetically controlled mineral dissolution and precipitation is calculated using transition
 266 state theory (Helgeson et al., 1984; Lasaga, 1984):

$$R_m = A_{w,m} K_m \left(1 - \frac{IAP}{K_{eq}}\right) \quad (1)$$

267 where R_m is the dissolution/precipitation rate of the mineral m (mol/s), $A_{w,m}$ is the wetted sur-
 268 face area of the mineral m per volume of porous media (m^2/m^3), K_m is the intrinsic rate constant
 269 ($\text{mol}/(\text{m}^2/\text{s})$), IAP is the ion activity product for the reaction, and K_{eq} is the thermodynamic equi-
 270 librium constant. The wetted surface area depends on groundwater storage through the following
 271 equation (Clow & Mast, 2010):

$$A_{w,m} = A_m S_w^n \quad (2)$$

272 where A_m is the total surface area of the mineral m per volume of the porous media under the fully
 273 saturated condition, S_w is the water saturation (m^3 water per m^3 pore space) and n is equal to 2/3
 to represent the surface area to volume ratio of mineral grains (Mayer et al., 2002). The RT module
 and Flux-PIHM are coupled through the minerals' specific surface area (*SSA*) dependence on soil
 moisture.

The governing equation for reactive transport of an arbitrary solute m is as follows:

$$V_i \frac{d(S_{w,i} \theta_i C_{m,i})}{dt} = \sum_{j=N_{i,1}}^{N_{i,x}} (A_{ij} D_{ij} \frac{C_{m,j} - C_{m,i}}{I_{ij}} - q_{ij} C_{m,j}) + R_{m,i} \quad m = 1, \dots, np \quad (3)$$

274 where V_i is the total volume of grid cell i ; $S_{w,i}$ is the water saturation (m^3 water per m^3 pore space),
 275 θ_i is the porosity (m^3 pore space per m^3 total volume); $C_{m,i}$ is the aqueous concentration of species
 276 m (mol/m^3 water); $N_{i,x}$ is the index of the neighboring elements of grid cell i , with the subscript
 277 x is set to two for unsaturated zone fluxes (infiltration and recharge) and four for saturated zone
 278 fluxes (recharge and lateral flow), respectively; A_{ij} is the interface area between the grid cell i and
 279 its neighbor cell j (m^2); D_{ij} is the dispersion/diffusion coefficient (m^2/s), I_{ij} is the distance between
 280 the center of the neighboring grid cells; q_{ij} is the volumetric flow rate across A_{ij} (m^3/s); and np is
 281 the total number of independent solutes.

282 In the model, a major assumption is that groundwater boundaries align with the surface watershed
 283 boundary, which prevents solutes from entering the watershed via groundwater. Another simplifica-
 284 tion is that in the model version used here, lateral "groundwater" flow represents the combination
 285 of shallow soil water interflow and groundwater flow. Further, all groundwater is eventually routed
 286 laterally into the stream and exits the watershed as surface discharge.

287 Full details about RT-Flux-PIHM can be found in Qu and Duffy (2007); Shi et al. (2013); Bao et al.
 288 (2017).

289 4.2 Model Setup

290 4.2.1 Hydrological and Transport Processes

291 The model simulations using RT-Flux-PIHM version 0.10.0 alpha were applied from June 2015
 292 - June 2016. Implementation of the Gavilan Machay model domain and hydrological processes

293 follows Saberi et al.'s (2019) implementation of Flux-PIHM; a brief summary is provided here. To
 294 include ice melt in the simulation, a separate temperature-index module was added to the model.
 295 Glacial melt was estimated under the assumption that ablation occurs over the glacierized grid cells
 296 below the equilibrium line altitude (ELA) at 5050 m a.s.l (La Frenierre & Mark, 2014). The PIHMgis
 297 software (Bhatt et al., 2014) was used to discretize the domain into 188 triangular cells. Land-
 298 cover was set as grassland at the lowest elevations to represent páramo, barren/sparsely vegetated for
 299 the mid-altitude, and perennial ice/snow for the ice-covered areas (Figure 2a). Built-in land cover
 300 parameters from Noah-LSM were used for each land-cover type. Leaf area index for the vegetated
 301 parts of the watershed were from MODIS (Vermote, 2015).
 302 In Saberi et al. (2019), soil hydraulic parameters of Flux-PIHM were calibrated to stream discharge
 303 measurements and hydrochemical mixing model estimates of melt contributions. In this study, using
 304 RT-Flux-PIHM, soil hydraulic parameters were directly constrained using major ion concentrations
 305 in the stream and groundwater, in addition to stream discharge (Table 4).

306 4.2.2 Geochemical Processes

307 The RT module was implemented with equilibrium aqueous complexation reactions for major
 308 elements (Na^+ , Ca^{2+} , Mg^{2+} , chloride (Cl^-), and silica (SiO_2)) and pH, and with kinetic mineral
 309 reactions. Aqueous chemistry measurements were used to constrain mineral dissolution kinetic pa-
 310 rameters. The chemical concentrations at the GW-1 and GW-2 spring (groundwater) sampling points
 311 (Fig 2a) were used to establish two different initial groundwater geochemical conditions for the spin-
 312 up run, one for the vegetated portion of the watershed and the other for the bare soil/ice-covered
 313 portion of the watershed (Table 2). The model was run in a spin-up mode until species reached a
 314 steady state such that their concentrations did not change with time. Due to the approximate na-
 315 ture of the spin-up, averaged steady-state concentrations of groundwater in the vegetated cells and in
 316 the bare soil/ice-covered cells were used as spatially uniform initial conditions for these respective
 317 portions of the watershed in the final simulation. As shown in Table 2, the measured and spun-up
 318 initial concentrations were higher at lower elevations (grassland) (Figure 2a). Although glacier melt
 319 samples had slightly higher concentrations than precipitation samples, they were of similar orders
 320 of magnitude that were much lower than that of the groundwater and streamwater samples. This
 321 justified the use of the same geochemical composition for both precipitation and glacial melt in the
 322 model in order to simplify the implementation with only one forcing condition for the two types of
 323 inputs. Precipitation and glacier melt concentrations were assumed to be constant over space and
 time.

	Precipitation	Glacial Melt	Grassland (Observed)	Grassland (Initial Condition)	Sparsely Vegetated and Ice-covered (observed)	Sparsely Vegetated and Ice-covered (initial condition)
Elemental Species (mol/l except for pH)						
pH	6.3	5.76	5.64	5.5	5.51	5.5
Na^+	2.78×10^{-5}	4.71×10^{-5}	2.41×10^{-4}	5.1×10^{-5}	1.94×10^{-4}	4.2×10^{-5}
Ca^{2+}	2.27×10^{-5}	3.36×10^{-5}	2.11×10^{-4}	2.1×10^{-5}	1.9×10^{-4}	2.11×10^{-5}
Mg^{2+}	1.43×10^{-6}	7.45×10^{-5}	2.59×10^{-4}	2.5×10^{-5}	1.8×10^{-4}	1.8×10^{-5}
Cl^-	3.77×10^{-5}	4.12×10^{-5}	9.04×10^{-5}	6.2×10^{-6}	5.81×10^{-5}	9.1×10^{-6}
SiO_2	0	0	2.54×10^{-4}	2.3×10^{-5}	2.93×10^{-4}	2.8×10^{-5}

Table 2: Initial chemical composition of groundwater, precipitation, and glacial melt in different portions of the Gavilan Machay watershed. The same chemical composition was applied to both bare soil and ice-covered areas. Precipitation concentrations were used for both glacial meltwater and precipitation in the simulations.

325 4.2.2.1 Non-reactive Chloride Processes

326 Due to the absence of chloride-containing minerals in the XRD results, we used Cl^- as a non-
 327 reactive tracer, which we assume enters the watershed through wet atmospheric deposition. The
 328 higher Cl^- concentrations in the groundwater relative to precipitation and melt (Table 2) likely oc-

329 curs through ET. Because this process occurs in the absence of geochemical reactions, we used Cl^-
 330 as a tracer to evaluate the hydrological processes controlling the spatiotemporal variability of hydro-
 331 chemistry in the watershed.

332 4.2.2.2 Reactive Sodium, Calcium, and Magnesium Processes

333 In addition to atmospheric deposition and ET, concentrations of reactive ions, including Na^+ ,
 334 Ca^{2+} , and Mg^{2+} , are also influenced by mineral dissolution from soil and rock containing feldspar
 335 and pyroxenes minerals. Albite ($\text{NaAlSi}_3\text{O}_8$) and diopside ($\text{CaMgSi}_2\text{O}_6$) were chosen as represen-
 336 tative model minerals from these groups, respectively, because they were prevalent across multiple
 337 samples, and the choice of two minerals enabled us to most simply produce observed concentrations
 338 throughout the watershed (Table 1). Other minerals containing elements with very low observed
 339 solute concentrations (e.g., Iron (Fe) and Manganese (Mn)) were not considered in order to focus on
 340 major elements. We represent kinetic dissolution of albite and diopside using parameters from lit-
 341 erature with further manual adjustments to reproduce observed streamwater and groundwater solute
 342 concentrations and stream discharge (Table 3).

Mineral Dissolution	$\log_{10}K_{\text{eq}}^a$	$\log_{10}k^b$	SSA(m^2/g) ^c
$\text{NaAlSi}_3\text{O}_{8(s)} (\text{Albite}) + 4\text{H}_2\text{O} + 4\text{H}^+ \rightarrow \text{Na}^+ + \text{Al}^{3+} + 3\text{H}_4\text{SiO}_4$	2.76	-10.9 (-9.89 – -11.9)	0.075 (0.02 – 1.09)
$\text{CaMgSi}_2\text{O}_{6(s)} (\text{Diopside}) + 2\text{H}_2\text{O} + 4\text{H}^+ \rightarrow \text{Ca}^{2+} + \text{Mg}^{2+} + 2\text{H}_4\text{SiO}_4$	20.96	-13.2 (-9.95 – -14.24)	0.086 (0.001 – 2.3)

^a K_{eq} from the database EQ3/6 (Wolery, 1992)

^b Calibrated dissolution rate constants, which fall within the range of values presented in Brantley et al. (2008) (shown in parentheses).

^c Calibrated soil mineral specific surface area (SSA) values; these fall within the range of values presented in Brantley et al. (2008) (shown in parentheses).

Table 3: Dissolution reactions and kinetic and thermodynamic parameters for minerals included in the model. For comparison, values in parentheses are the range found in (Brantley et al., 2008).

343 4.3 Model Scenarios

344 The model was implemented for three different scenarios. In the first scenario, Na^+ , Ca^{2+} , and
 345 Mg^{2+} were simulated as non-reactive ions along with Cl^- , in order to isolate the control of hydro-
 346 logical processes. In the second scenario, mineral dissolution was included to assess the impact of
 347 geochemical processes on the concentrations of Na^+ , Ca^{2+} , and Mg^{2+} . To evaluate the role of glacier
 348 melt in controlling current hydrochemical conditions, we also tested a third scenario that includes
 349 geochemical processes without glacial meltwater. In the scenarios with mineral dissolution (2 and
 350 3), we chose Na^+ as the representative diagnostic solute among the three dominant ions observed in
 351 the watershed (Na^+ , Ca^{2+} , Mg^{2+}); simulation results of other ions were qualitatively similar to Na^+
 352 results.

353 4.4 Model Calibration

354 Continuous hourly measured stream discharge from June 2015-June 2016 and the discrete mea-
 355 surements of Na^+ , Ca^{2+} , Mg^{2+} , and pH on June 15, 2015, June 15, 2016, and February 20, 2017
 356 were used for the model calibration. Na^+ is involved in albite dissolution, and Ca^{2+} and Mg^{2+} par-
 357 ticipates in diopside dissolution. To reproduce the stream discharge and major ion concentrations in
 358 groundwater and stream water, soil hydraulic properties (for the vegetated, non-vegetated, and ice-
 359 covered portions of the watershed), and mineral specific surface area were manually tuned. Monte

360 Carlo simulations with perturbations added to the final calibrated soil hydraulic parameters (shown
 361 in Table 4) were carried out to evaluate the sensitivity of the model performance to a range of plau-
 362 sible soil parameters and to provide a rough representation of uncertainty associated with the final
 363 simulations (details in the Supplementary Information, Section S-1).

	KINFV (m/s)	KSATV (m/s)	KSATH (m/s)	Porosity	Residual Moisture	α (1/m)	β (-)
Ice-covered	1.64E-7	4.56E-8	4.56E-7	0.296	0.05	0.412	1.038
Sparsely Vegetated	1.74E-7	4.85E-8	4.85E-7	0.296	0.05	0.437	1.038
Grassland	1.87E-7	5.27E-8	5.27E-7	0.297	0.05	0.469	1.039

Table 4: Parameters calibrated to match observed discharge and major ion concentrations in stream water and groundwater. Parameters include hydraulic conductivities for vertical infiltration (KINFV), vertical saturated flow (KSATV), horizontal saturated flow (KSATH), porosity, residual soil moisture, and shape parameters (α and β) for the van Genuchten moisture retention curve: $\theta = \theta_{res} + porosity \times \left(\frac{1}{1+|\alpha\psi|^\beta} \right)^{(1-\frac{1}{\beta})}$, with water content θ and pressure head ψ . The comparison of new versus previous soil hydraulic estimations from Saberi et al. (2019) are shown in the Supplementary Information, Table S2.

364 We relied on the widely used Nash-Sutcliffe efficiency (NSE) approach (Nash & Sutcliffe, 1970)
 365 to quantify model performance. Model results are considered satisfactory if $0 < NSE < 1$, with $NSE = 1$
 366 as an indicator of a perfect match between observations and simulations (Moriassi et al., 2007). The
 367 traditional NSE is used here, which is calculated as follows (Nash & Sutcliffe, 1970):

$$NSE = 1 - \frac{\sum_{i=1}^n e_i^2}{(O_i - O_m)^2} \quad (4)$$

368 where, e_i is the error (Observed_{*i*}-Simulated_{*i*}) for location and time i , n is the number of measure-
 369 ments, O_i is the measurement at location and time i , and O_{mean} is the mean of all measurements.
 370

371 4.5 C-Q Power Law Model

372 The concentrations (C) of non-reactive and weathering-derived solutes exported from a water-
 373 shed may depend on stream discharge (Q) (Shanley et al., 2011; R. F. Stallard & Murphy, 2014) or
 374 remain relatively time-invariant (chemostatic) depending on the processes within the watershed con-
 375 trolling them (Hem, 1985; Johnson et al., 1969; Godsey et al., 2014; Li et al., 2017). The relationship
 376 between solute concentrations and stream discharge is often fit to a power law relationship (Godsey
 377 et al., 2009):

$$C = aQ^b \quad (5)$$

378 where a and b are fitted parameters. b has been found to vary from -1 to +0.4 (Godsey et al., 2009;
 380 Herndon et al., 2015). The C-Q relationships are often considered chemostatic when b ranges be-
 381 tween -0.2 and +0.2, while pure dilution (non-chemostatic end-member) occurs when b is equal to
 382 -1.

383 To investigate the influence of glacial melt on the hydrochemistry of the watershed, we compare C-Q
 384 power law model fit to simulation results with meltwater and without meltwater. Although C-Q anal-
 385 ysis is typically applied to continuous measurements, here we rely on model simulations to overcome
 386 data sparsity and to explore different scenarios.

387 5 Results and Discussion

388 5.1 Calibration Results

389 Calibration results for geochemical reaction parameters and soil hydraulic parameters are shown
 390 in Tables 3 and 4, respectively. Simulated stream discharge matches observed discharge with an NSE

391 coefficient of 0.87, which indicates that the model performance is satisfactory (Figure 3a). Constraining
 392 the model simulations on observed hydrochemical concentrations in addition to stream discharge
 393 resulted in lower calibrated porosity and van Genuchten parameters than those used in Saberi et al.
 394 (2019) (Table S2). As noted above, in Saberi et al. (2019), only discharge data were directly used
 395 in the parameter calibration, while hydrochemical data were indirectly considered through model
 396 constraints on estimates of melt and groundwater contributions from a mixing model. The newly
 397 calibrated hydraulic parameters in this study resulted in lower groundwater retention and correspond-
 398 ingly higher groundwater contribution to streamflow.

399 The calibrated model results further show that lateral groundwater flow, which contains both pre-
 400 cipitation and glacial meltwater, contributes on average 78% of streamflow (Figure 3a), with sur-
 401 face runoff contributing the remaining 22%. In comparison, Saberi et al. (2019) determined a 45%
 402 groundwater contribution to streamflow using Flux-PIHM, which was calibrated to be consistent
 403 with mixing model estimates of melt and groundwater contributions (Figure 4a). The hydrochemi-
 404 cally constrained RT-Flux-PIHM model in this study and the mixing model in Saberi et al. (2019)
 405 use the same hydrochemical observations from the Gavilan Machay watershed, but the difference in
 406 the groundwater contribution estimates arises because the mixing model relied on few samples from
 407 readily accessible springs in lower reaches of the watershed to represent the groundwater end-member
 408 throughout the entire watershed. In contrast, the distributed RT-Flux-PIHM model appropriately ac-
 409 counts for spatially variable groundwater concentrations, which differ substantially with elevation as
 410 groundwater moves from headwater areas toward the discharge point, due to increasing contact time
 411 with reactive minerals. Comparison of these results demonstrates the importance of hydrochemi-
 412 cal model constraints in addition to hydrological constraints. In the RT-Flux-PIHM results, stream
 413 discharge closely follows the temporal trends of groundwater discharge to the stream (coefficient of
 414 correlation of 0.79), indicating that simulated stream flow is predominantly controlled by groundwa-
 415 ter (Figure 3a). The lateral groundwater flow to the stream is further positively correlated with the
 416 precipitation plus melt over time (coefficient of correlation of 0.65), which suggests that precipitation
 417 and ice melt that infiltrate travel relatively fast to the stream such that their temporal variability is not
 418 significantly dampened and lost in the subsurface (Figure 3b).

Direct model calibration to hydrochemical data not only improved the constraint on groundwater
 contributions to the stream, but also on melt-groundwater interactions. The estimate of discharge
 originating from meltwater that first infiltrates and travels as groundwater before flowing to streams
 increased from 16% to 37% after constraining the model on hydrochemical observations (Figure 3c
 and 4b). Following Saberi et al. (2019), the percent melt contribution to the groundwater is calculated
 using simulation scenarios with and without ice melt:

$$\%MeltInGroundwater = \frac{Groundwater_{WithIceMelt} - Groundwater_{WithoutIceMelt}}{Groundwater_{WithIceMelt}} \quad (6)$$

419 where $Groundwater_{WithIceMelt}$ and $Groundwater_{WithoutIceMelt}$ is the lateral groundwater contri-
 420 bution to the stream in scenarios with and without ice melt, respectively. New hydrochemically
 421 constrained simulations show that as the temperature increases during the El Niño event, the ice melt
 422 contribution to the groundwater increases (Figure 3d).

423 Overall, this result demonstrates that incorporating hydrochemical data in the model calibration con-
 424 strains flow pathways and impacts partitioning of both stream discharge and meltwater. Constraining
 425 the model simulations on hydrochemical data results in higher meltwater contribution to groundwa-
 426 ter and higher groundwater contribution to the streamflow (Figure 4).

427 To evaluate the role of geochemical reactions in simulating observed hydrochemical conditions, we
 428 compared Na^+ , Ca^{2+} , and Mg^{2+} concentrations in groundwater in scenarios with and without min-
 429 eral dissolution. The results show that without mineral dissolution, meteoric and melt inputs and
 430 ET could account for only 14-16% of the time-average concentrations, and that mineral dissolution
 431 was needed in the model to match observed groundwater concentration ranges at different locations
 432 within the watershed (Figure 5).

433 Figure 6 shows the calibrated concentrations of all three major ions at the outlet, which match
 434 reasonably well with measured concentrations during the 2015 and 2016 field campaigns. The cali-

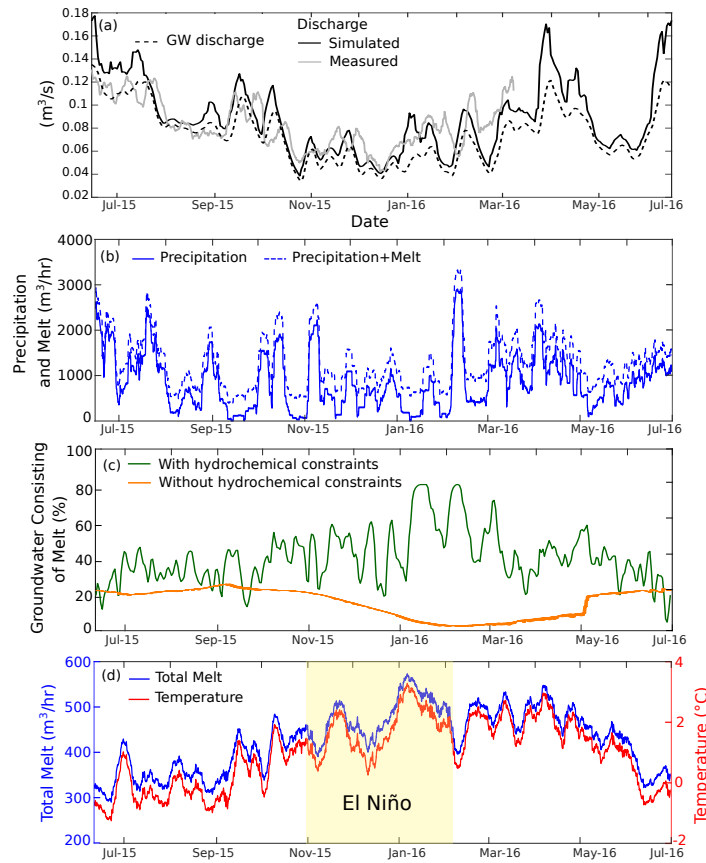


Figure 3: Temporal variability of a) simulated stream discharge, measured stream discharge, and groundwater discharge to the stream, b) precipitation (solid line) and precipitation + ice melt (dashed line), c) percentage of groundwater that constitute ice melt, d) average air temperature over the ablation zone (glacier-covered areas below the ELA (5050 m a.s.l.)) and simulated glacier melt production. The blue box demonstrated the time period during which an El Niño event occurred over the watershed. The x-labels indicate the start of the corresponding month.

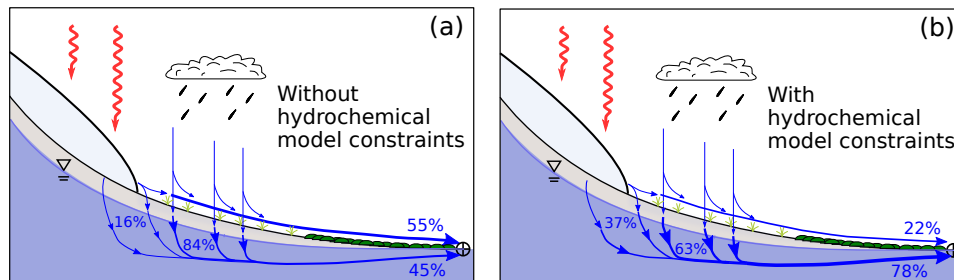


Figure 4: Groundwater partitioning between glacier melt and precipitation inputs, and stream discharge partitioning between surface runoff and groundwater. Model results for two cases are shown: a) without directly constraining the model on hydrochemical data versus b) with direct constraints on hydrochemical data.

435 bration results for the Na^+ concentrations along the stream sampling points SW-1, SW-2, and SW-3
 436 (locations shown in Figure 2a) are presented in the Supplementary Information (Figure S2).

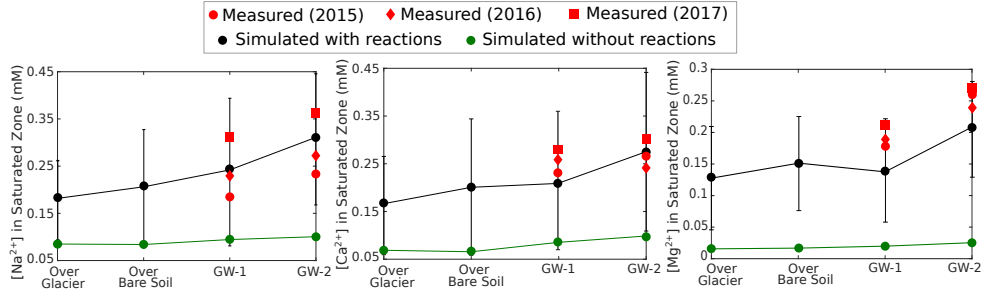


Figure 5: Simulated groundwater concentrations of Na^+ , Ca^{2+} , and Mg^{2+} along an elevation gradient for two different scenarios, with and without geochemical reactions, along with measured ion concentrations. Ion concentrations were measured at the GW-1 and GW-2 spring locations (locations shown in Figure 2a). Simulated concentrations averaged over glacierized (ranges from 5300-6280 m.a.s.l) and bare soil cells (ranges from 4600-4900 m.a.s.l) were chosen to demonstrate the changes in concentrations simulated in the upper and middle parts of the watershed, where we lack groundwater samples. The error bars around the calibrated simulation results with reactions show a plus or minus one standard deviation interval from the Monte Carlo uncertainty simulations.

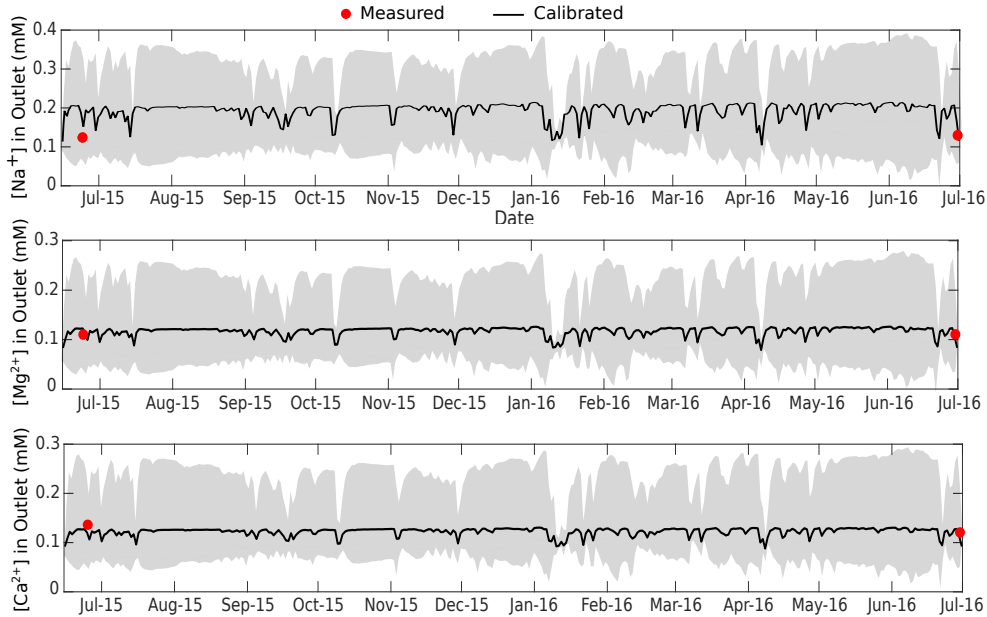


Figure 6: Simulated Na^+ , Ca^{2+} , and Mg^{2+} in the outlet (calibrated result in black lines) compared to the measured concentrations at the SW-4 site (Figure 2a). Gray shaded areas show a plus or minus one standard deviation interval from the Monte Carlo uncertainty simulations.

437

5.2 Hydrological Controls on Subsurface Chemistry

To isolate the impact of hydrological processes on the hydrochemistry of the watershed, we examined Cl^- transport and its groundwater concentration variations arising from different hydrologic fluxes, including infiltration (diluting effect) and ET (concentrating effect). A simple mass balance assuming steady-state helps demonstrate the relative controls of the hydrologic fluxes on groundwater concentrations:

$$C_p \times \text{Infiltration} = C_g \times (I - ET) \quad (7a)$$

$$I = (\text{Precipitation} + \text{Melt}) - \text{Runoff} - \text{SurfaceEvaporation} \quad (7b)$$

where C_p is the Cl^- concentration in precipitation, C_g is the average Cl^- concentration in the saturated and unsaturated zones, I is infiltration, and ET is evapotranspiration. Eq. 7a can be rearranged to show the dependence of groundwater concentrations of Cl^- on the ratio of ET to infiltration (higher ratio results in higher groundwater concentration):

$$C_g = \frac{C_p}{\left(1 - \frac{ET}{I}\right)} \quad (7c)$$

The model shows that the highest ET occurs within the vegetated parts of the watershed (Figure 2 and Figure 7a), with a maximum annual average of 2.4 mm/day. High ET and relatively lower infiltration rates in the vegetated area (Figure 7b) results in high ET to infiltration ratios (Figure 7c), which lead to increased Cl^- concentrations in groundwater (maximum of 0.065 mM) in these regions (Figure 7d).

Within the ice-covered area, not only is ET lower than in vegetated regions (Figure 7a), but infiltration rate is also higher (Figure 7b) due to high glacial melt rates, which are greater than the precipitation rate in most of the watershed. This results in very low ET to infiltration ratios (Figure 7c), thus generating some of the lowest concentrations in the watershed (Figure 7d).

5.3 Geochemical Controls on Hydrochemistry

5.3.1 Temporal Patterns

The sources of Na^+ in the model simulations include Na^+ production by mineral dissolution (R_p) and Na^+ input from glacial melt and rainfall (R_{mr}). R_p is the Na^+ production rate through albite dissolution, which was calculated by:

$$R_p = \frac{C_{Albite_t} - C_{Albite_{t-1}}}{dt} \quad (8)$$

where the increment in time is 1 day and C_{Albite} is the concentration of albite at time t . The Na^+ input from glacial melt and rainfall (R_{mr}) is the product of the melt plus precipitation rate, the Na^+ concentration in the precipitation, and the grid cell area. Watershed-scale values for R_p and R_{mr} were determined by summing over all grid cells. The Na^+ export rate (R_e) is the product of stream discharge and Na^+ concentrations at the stream outlet. As can be seen in Figures 8a and b, the simulated R_e primarily follows the stream discharge pattern (correlation coefficient of 0.88), which suggests that the discharge is the stronger driver of export rate variability over time than the concentration of Na^+ at the outlet. This is because Na^+ concentration at the outlet is relatively constant year-round (coefficient-of-variation of 13%) compared to the variability in discharge (coefficient-of-variation of 44%) (Figure 7c).

The low simulated variability of Na^+ concentrations at the outlet is largely due to groundwater-related processes. The importance of the subsurface is evident when comparing the different Na^+ input and output magnitudes. In the model, the production of Na^+ via mineral dissolution (average 1.68×10^9 mg/d) is much higher than meteoric and glacier melt inputs of Na^+ (average 1.8×10^7 mg/d), contributing to the vast majority of Na^+ export at the outlet (average 3.6×10^8) (note that excess Na^+ inputs are added to groundwater storage of Na^+ over the simulation period). However, during the dry period (November-February), even though lower groundwater storage (Figure 3b) leads to a decline in Na^+ production (Figure 8b), high ET concentrates Na^+ in groundwater (Figure 8a and c). During the wet periods (June-October and March-May), higher groundwater storage (Figure 3b) results in higher wetted surface area of minerals, thereby supporting higher albite dissolution rates and Na^+ production, which somewhat compensates for dilution by high precipitation and melt events (Figure 8b). However, overall, ET has a prevailing effect on concentrations during the wet period as well. Na^+ production by albite dissolution to some degree modulates concentrations during the wet period,

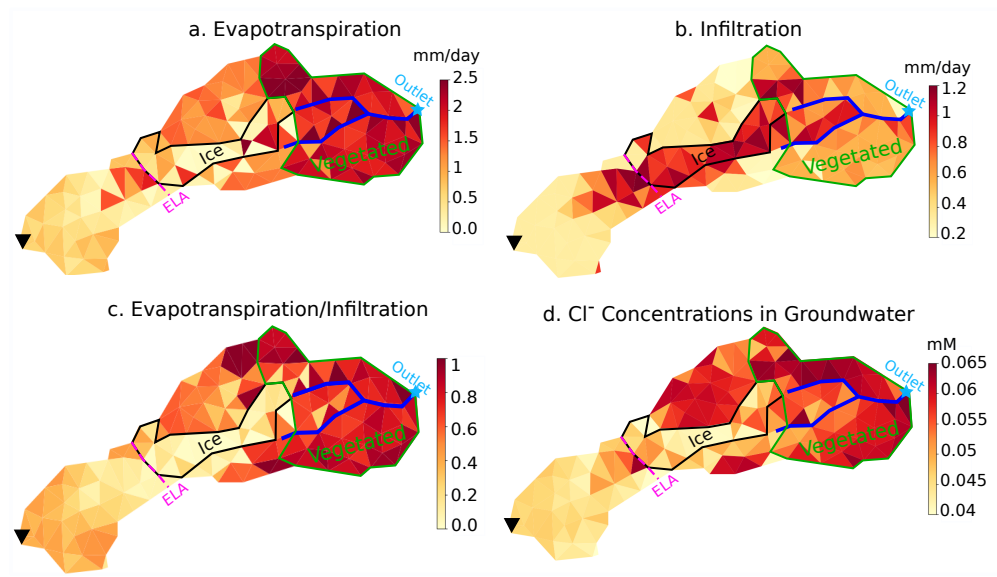


Figure 7: Time-averaged model results over each grid cell. a) ET, b) infiltration (as defined in text), c) ratio of ET to infiltration, and d) Cl^- concentrations averaged over saturated and unsaturated zones. The black triangle shows the peak of Volcán Chimborazo (6280 m a.s.l.). The dashed pink line represents the ELA at 5050 m a.s.l. The black outline indicates the glacierized grid cells below the ELA, in which glacier melt is applied in model. The green outline identifies the vegetated part of the watershed. The blue line shows the stream channel, and the blue star indicates the outlet.

475 but the concentrations in groundwater are still lower than those during the dry period due to lower
 476 ET during the wet period (Figure 8c).

477 Higher simulated variability in stream chemistry (coefficient-of-variation of 13%) compared to ground-
 478 water chemistry (coefficient-of-variation of 2%) suggests that surface water dilution via runoff contri-
 479 bution to the stream may still have an impact (Figure 8c). However, the temporal variation of stream
 480 chemistry is primarily controlled by the percentage groundwater contribution to the stream (correla-
 481 tion coefficient of 0.79) (Figure 8c). As noted above (Section 5.1), lateral groundwater is positively
 482 correlated with precipitation plus melt inputs, which together indicates that large precipitation and
 483 melt events promote solute export via flushing of solutes stored in groundwater.

484 5.3.2 Spatial Patterns

485 Figure 9 shows the spatial distribution of simulated hydrological and geochemical variables, aver-
 486 aged over separate wet and dry seasons, to probe different processes controlling the spatial variabil-
 487 ity of the hydrochemistry over different hydrological conditions. Throughout the year, ET is highest
 488 over the vegetated parts of the watershed due to plant transpiration, and soil moisture is highest in
 489 the convergent areas and adjacent to the stream (Figure 9). The spatial pattern of Na^+ concentra-
 490 tions in groundwater follows both ET and Na^+ production rates in the model, which suggests that these
 491 two fluxes have a combined impact on the spatial variability of Na^+ in groundwater. Multivariate
 492 regression analysis showed that on average (throughout the year and over the entire watershed), 69%
 493 of the spatial variability in groundwater concentrations can be explained by ET and 31% by produc-
 494 tion via albite dissolution, with precipitation and melt inputs having negligible impact.

495 Interestingly, while correlation results show that Na^+ production via albite dissolution plays a sec-
 496 ondary role in explaining the spatial variability of Na^+ concentrations in groundwater relative to
 497 ET, production is in fact the predominant controller of the spatial mean concentration in the model.
 498 Specifically, the mean groundwater Na^+ concentration over the watershed increases nearly six-fold
 499 with albite dissolution in the model, from 0.03 mM to 0.17 mM. This result is not surprising consid-

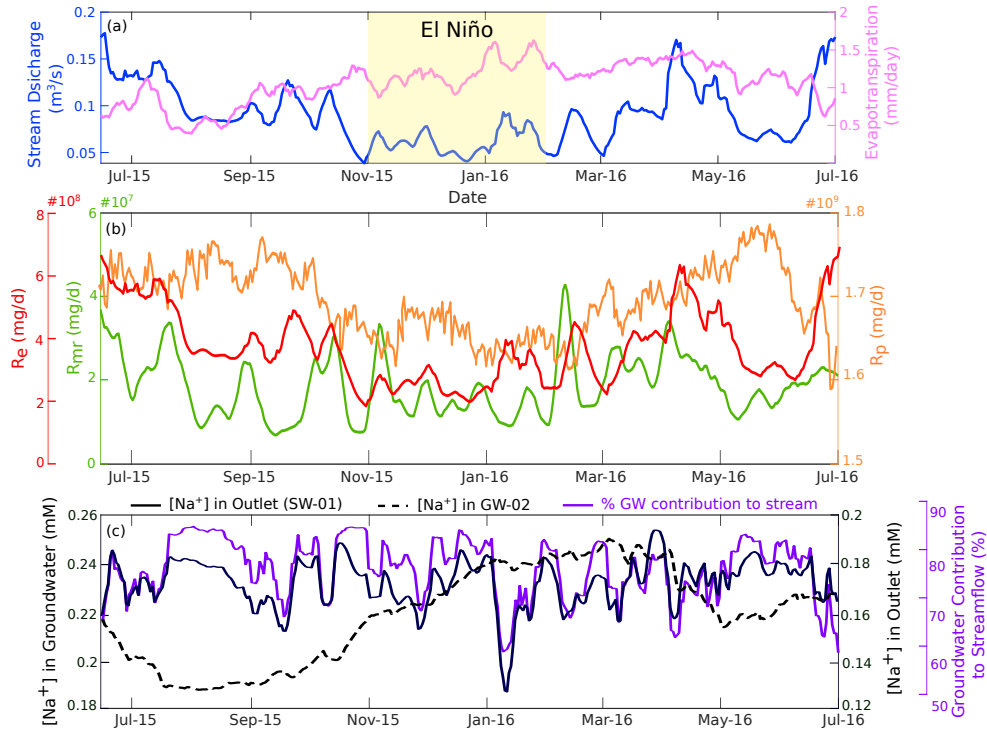


Figure 8: Temporal variability of a) stream discharge and ET, with the warm and low-precipitation El Niño period shaded yellow; b) Na^+ input by precipitation and melt events (R_{mr}), Na^+ export rate at the outlet (R_e), and Na^+ production rate by albite dissolution (R_p); and c) Na^+ concentration in groundwater (at sample site GW-2 shown in Figure 2a), Na^+ concentration in the outlet (sampling site SW-4 shown in Figure 2a), and percentage of groundwater contribution to streamflow. The blue box demonstrated the time period during which an El Niño event occurred over the watershed.

500 ering total watershed results in Figure 8 show that production comprises the vast majority of all mass
 501 inputs of Na^+ into the watershed. Further, when compared to ET, dissolution appears to account for
 502 more of the overall concentration gradient with topography around the stream channel. Calibrated
 503 simulations with mineral dissolution show a groundwater concentration gradient of 0.045 mM/km
 504 a.s.l. for Na^+ from below the glacierized headwaters at 5200 m a.s.l. to below the lower stream reach
 505 at 4100 m a.s.l. (GW-2) (Figure 3). In comparison, the model scenario without mineral dissolution
 506 resulted in less than half the concentration gradient (0.018 mM/km a.s.l.) over the same interval,
 507 demonstrating that alone, ET effects explain a smaller portion of the concentration changes over the
 508 full watershed extent of the stream channel. Together, the spatial analysis shows that production via
 509 mineral dissolution plays the major role in explaining spatial mean concentrations of reactive solutes
 510 and concentration gradients along the full extent of the stream channel, while ET is the better pre-
 511 dictor of finer scale spatial variability among all grid cells.

512

To examine the processes behind the relative contributions of ET and mineral dissolution to solute concentrations across the watershed, we looked at potential interactions between ET and dissolution. For example, the apparent control of ET on the finer scale spatial variability of Na^+ groundwater concentrations could in fact be driven by production, because higher ET can lead to lower flow and longer contact times that facilitate mineral dissolution. However, a weak spatial correlation between ET and Na^+ production (correlation coefficient of 0.15) suggests that this is not a major phenomenon in the model simulations. Instead, Na^+ production strongly follows soil moisture content (correlation coefficient of 0.89 over space), which does lead to higher groundwater concentrations along the

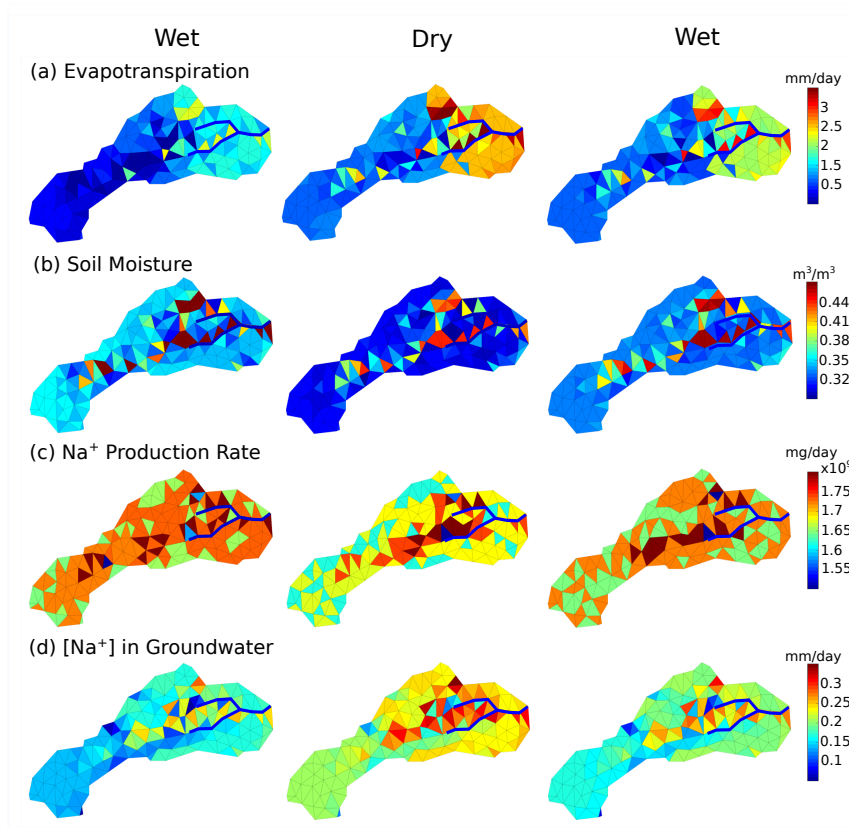


Figure 9: a) ET, b) Soil Moisture, c) Na^+ production rate, and d) Na^+ concentration in groundwater averaged over three time periods (June-October, November-February, March-May).

stream and in convergent areas where soil moisture content is close to the saturation (Figure S3). However, it appears that overall spatial variability of concentrations among all grid cells is mostly controlled by ET via direct removal of soil moisture. Further evaluation reveals that some of the apparent dissolution controls on large-scale Na^+ groundwater concentrations (spatial mean and gradient over the extent of the watershed) in fact involve ET processes. This can be understood with the following steady-state mass balance equation for reactive solutes, which is a straightforward extension of the non-reactive case for Cl^- (equations 7a and 7c):

$$C_g = \frac{R_p + C_p \times I}{I - ET} \quad (9a)$$

$$C_g = \frac{\frac{R_p}{I}}{1 - \frac{ET}{I}} + \frac{C_p}{1 - \frac{ET}{I}} \quad (9b)$$

513 where C_g is the Na^+ concentration in groundwater, R_p is the Na^+ production rate through albite
 514 dissolution, C_p is the Na^+ concentration in precipitation and meltwater, I is the infiltration, and ET
 515 is evapotranspiration. From the first term on the right hand side of equation 9b, it can be seen that
 516 with $ET > 0$, the Na^+ input from dissolution (R_p) is amplified by a factor of $\frac{1}{1 - \frac{ET}{I}}$ when determin-
 517 ing the groundwater concentration. This multiplicative amplification effect likely explains why ET
 518 plays such an important role in controlling the fine scale spatial variability throughout the watershed,
 519 even though dissolution serves as the major source of solute mass over the watershed. This interac-
 520 tion underscores the importance of representing both geochemical and hydrological processes when

521 considering hydrochemical controls in a watershed. Our results also show that in heterogeneously
522 vegetated watersheds, such as those in high mountain environments with a discrete vegetation line,
523 ET variability can play a much larger role in controlling hydrochemical variability compared to sites
524 with relatively homogeneous land cover and ET (e.g., Li et al. (2017); Zhi et al. (2019)).

525 Broadly throughout the watershed, high soil moisture results in high Na⁺ production rates during the
526 wet seasons, with opposite results in the dry El Niño period (Figure 9a, b, and c). However, as noted
527 with the time series results for watershed-scale fluxes in Figure 8, Na⁺ concentrations in ground-
528 water were on average highest during this dry period due to high ET and low contribution of dilute
529 precipitation and ice melt to the watershed (Figure 9a and d). Spatial results further demonstrate that
530 over the dry period, the heterogeneity of the soil moisture content and production increases over the
531 watershed, with convergent areas and stream valleys having much higher productivity relative to the
532 rest of the watershed.

533 **5.4 Control of Glacier Meltwater on Na⁺ Production and Export**

534 **5.4.1 C-Q Power Law Model**

535 For simulations with meltwater, the relationship between stream discharge and the simulated
536 Na⁺ concentrations at the outlet is considered to be chemostatic based on a C-Q slope of -0.08 on a
537 log-log scale (Fig 10a). However, in Gavilan Machay, various dilution events also occur, and nearly
538 all of these (especially those with lowest concentrations) correspond to times of high surface runoff
539 contribution to discharge (Figure 10b). In particular, peak runoff contributions drive these dilution
540 events, which can occur any time of the year (Figure 10c). In simulations without glacier melt, peak
541 discharge and surface runoff contributions to discharge decrease. Overall Na⁺ concentrations in
542 groundwater increase, and almost all of the strongest dilution events disappear (Figure 10d, e, and f),
543 making the C-Q relationship even more chemostatic (slope of -0.011 on a log-log scale) (Figure 10d).
544 Torres et al. (2015) also found the C-Q relationship in non-glacierized, steep Andean catchments to
545 be chemostatic, potentially due to higher erosion rates and correspondingly higher dissolution rates
546 during peak flow. Comparison of the two model scenarios suggests that glacier melt produces some
547 of the largest surface runoff events in Gavilan Machay. These events can produce diluting episodes in
548 an otherwise chemostatic environment in which precipitation events mobilize solutes from highly re-
549 active subsurface minerals. It can also be seen that the melt-driven dilution events can occur anytime
550 because of year-round ablation in the tropics (Figure 3d). This is distinct from temperate systems
551 where glacier melt does impose a strong seasonal control on the hydrochemistry of the watershed
552 (e.g. Lewis et al. (2012); Stachnik et al. (2016)).

553 These model results indicate that the C-Q patterns are driven by the relative control of two end-
554 member sources of water. Streamflow is primarily derived from two sources with distinct chemistry:
555 surface runoff with low Na⁺ concentrations and groundwater lateral flow with higher Na⁺ concen-
556 trations. In the with-ice meltwater scenario, melt inputs lead to times when the ratio of surface runoff
557 to groundwater contribution to the stream is very high, and this produces a diluting effect. A similar
558 behavior was observed in simulations at the Coal Creek study watershed, where the C-Q relationship
559 was found to depend on the switching dominance among three end-members (surface runoff, shallow
560 groundwater, and deep groundwater) and the distinction among their chemistries (Zhi et al., 2019).
561 Without ice melt, Gavilan Machay is governed by a single end-member, lateral groundwater flow,
562 which results in much more chemostatic conditions; this is similar to RT-Flux-PIHM findings by Li
563 et al. (2017) for the Shale Hills study watershed. Higher groundwater contributions to streamflow
564 generate steadier and higher stream concentrations, because of less dilution by surface runoff. These
565 findings suggest that after glaciers fully retreat, the concentrations of major ions and nutrients in the
566 stream may increase and stabilize, though exact changes will also depend on future precipitation and
567 temperature.

568 **5.5 Glacial Meltwater Influence on Hydrogeochemical Processes**

569 To further probe processes controlling the C-Q relationships as well as their downgradient impli-
570 cations, we examine catchment-scale production and export rates, and Na⁺ concentrations in ground-

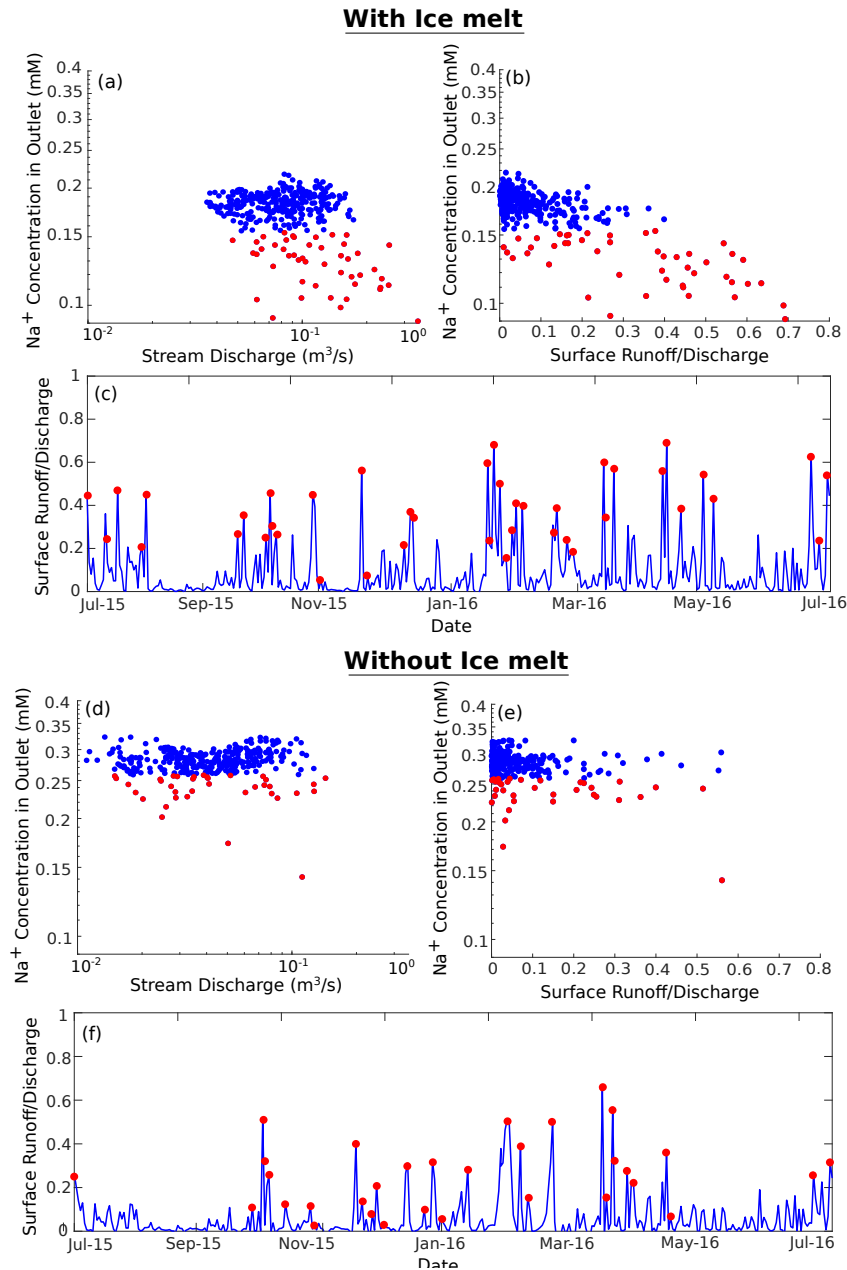


Figure 10: The relationship between simulated streamflow and simulated Na^+ concentrations at the outlet, with ice melt (a) and without ice melt (d). The relationship between the contribution of surface runoff to stream discharge (fraction of total discharge) and simulated Na^+ concentrations at the outlet, with ice melt (b) and without ice melt (e). The contribution of surface runoff to discharge (fraction of discharge) over time, with melt (c) and without ice melt (f). Red dots are the points at which the Na^+ concentrations in outlet are less than one standard deviation below the mean value due to high runoff contribution to streamflow.

571 water and at the outlet in the scenarios with and without glacier melt (Figure 10). For Na^+ , excluding
 572 ice melt leads to a decrease in Na^+ input with wet deposition (defined as the combined input from
 573 ice melt and precipitation) (Figure 11a), lower groundwater storage, lower soil water content, and

574 lower Na^+ production rate through albite dissolution (Figure 11b). However, even though wet deposition
 575 and production decrease, Na^+ concentrations in groundwater increases by 55% in the scenario
 576 without glacial melt (Figure 11d), due to the 170% higher ET to infiltration ratio (Figure 11c). The
 577 groundwater contribution to streamflow increases from 80% of the total discharge to 95% in the no
 578 melt scenario, although the absolute value of groundwater flow into the stream decreases by 41%
 579 without meltwater infiltration (Figure 11e). The increase in groundwater concentrations leads to
 580 51% higher Na^+ concentrations in the stream (Figure 11f), due to the dominance of groundwater
 581 contributions to total streamflow in no-melt scenario.

Even though Na^+ concentrations in streamflow are higher without meltwater, this cannot offset the

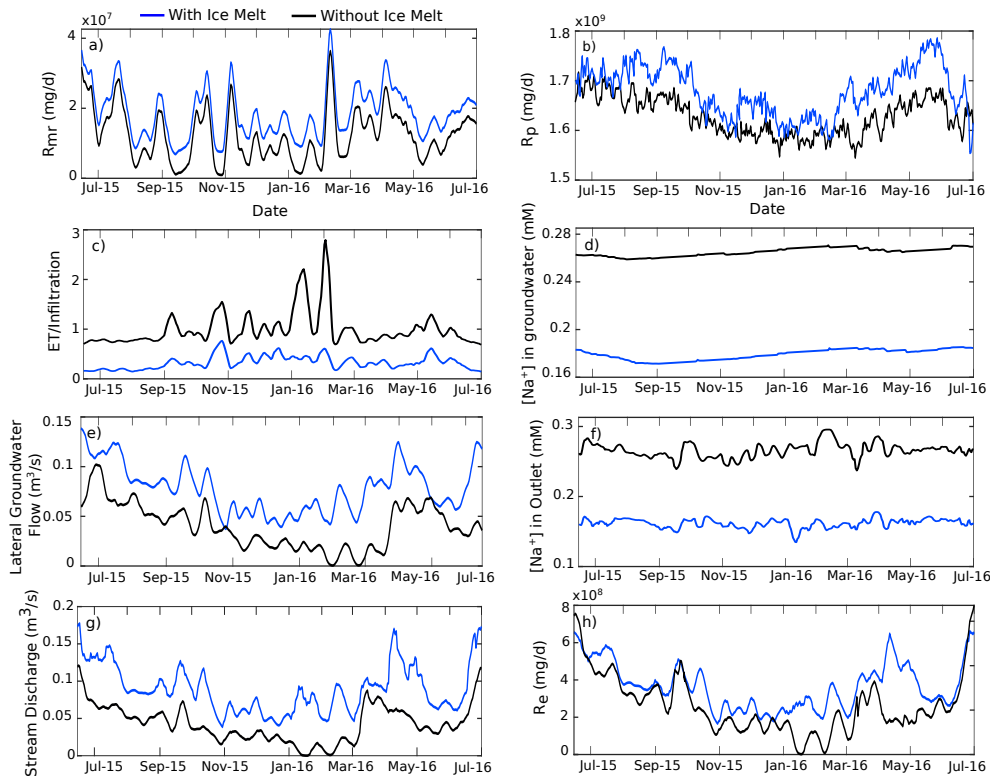


Figure 11: a) Na^+ input via melt and precipitation, b) Na^+ production rate via albite dissolution, c) the ratio of ET over infiltration, d) Na^+ concentrations in groundwater, e) groundwater discharge to the stream, f) Na^+ concentrations in the outlet, g) stream discharge, and h) Na^+ export rate (C^*Q). The blue line represents the scenario with melt and black like the scenario without glacial melt.

582 decrease in discharge when determining changes in export rates. Without glacier melt, time-average
 583 stream discharge decreases by 45% compared to the scenario with melt (Fig 11g). This results in
 584 23% lower export of Na^+ in the no-melt scenario (Figure 11h). This corresponds with findings based
 585 on a global data compilation that weathering yields are generally greater in glacierized watersheds
 586 compared to non-glacierized due to higher discharge, while solute concentrations are lower (Torres et
 587 al., 2017). Consistent with temporal variability findings in Section 5.3.1, the solute export rate con-
 588 ditions under melt versus no-melt scenarios appear to be controlled primarily by stream discharge
 589 and secondarily by groundwater contributions to streamflow.
 590

6 Summary and Conclusion

Our work highlights the complex hydrochemical responses of a tropical glacierized mountainous watershed on Volcán Chimborazo at different temporal and spatial scales controlled by hydrological and geochemical processes. Results indicate that model calibration to hydrochemical data in addition to hydrological data provides a better constraint on subsurface flow pathways. Our newly calibrated simulations show that total lateral groundwater flow contributed 78% of stream discharge, and that 37% of the total glacier melt directly contributes to groundwater flow.

Due to the presence of highly reactive silicate minerals, geochemistry plays an important role in controlling the hydrochemistry of the watershed. Mineral dissolution comprises most of the mass input of reactive ions such as Na^+ into the watershed, while wet deposition via precipitation and melt provides orders of magnitude less. As the major source, mineral dissolution controls the spatiotemporal mean groundwater concentration of reactive ions in the watershed, and it accounts for much of the gradient in groundwater concentrations with topography over the extent of the stream network.

Because mineral dissolution most directly influences groundwater chemistry, hydrological processes in the subsurface and groundwater-surface water interactions also play an important role in controlling the hydrochemistry of the watershed, including stream chemistry. Over the course of the year, dissolution rates are highest during the wet seasons, when high soil moisture allows for higher wetted surface area of minerals. But groundwater concentrations of reactive ions are relatively constant throughout the year (coefficient-of-variation of 2%) due to the offset effect of ET; ET is highest in the dry season, boosting concentrations even when production through mineral dissolution is low. Because groundwater flow to streams comprises a large fraction of total discharge, stream water concentrations of reactive ions are strongly controlled by groundwater contributions to the stream (temporal correlation coefficient of 0.79). Groundwater flow is fast, such that infiltration of large precipitation and melt events flush high solute concentrations from the subsurface into the stream. This flushing leads to higher temporal variability in stream water concentrations than groundwater concentrations (13% versus 2% coefficient-of-variation). This is still a much lower variability than in stream discharge (44% coefficient-of-variation). As a result, temporal variability in the export (concentration times discharge) of reactive ions is driven primarily by variations in discharge rather than concentration.

Although dissolution controls bulk amounts of reactive solutes in the watershed, ET plays the major role in determining the spatial variability in groundwater concentrations across the watershed. This spatial control by ET is especially pronounced because of the sharp gradient in vegetation, and similar effects may be expected in other steep, high-elevation watersheds with discrete vegetation lines. The spatial control by ET is likely heightened by interactions between ET and production via dissolution; the concentrating effect of ET includes a multiplicative amplification of the production rate based on the ratio of ET to infiltration. ET also serves as the dominant factor determining seasonal variability of groundwater concentrations; dry seasons have on average higher concentrations of reactive ions due to concentrating effects, despite lower production rates.

Because of year-round ablation in the tropics, glacier melt does not appear to be an important seasonal driver of hydrochemical variability. However, glacier melt does exert a unique influence on the C-Q relationship in the watershed. A model scenario test that omits glacier melt inputs exhibits strongly chemostatic behavior, consistent with past studies in non-glacierized, steep Andean watersheds in the tropics (Torres et al., 2015). In comparison, simulations with glacier melt have higher peak surface runoff, and times of high surface runoff contributions to streamflow produces strong dilution episodes superimposed on an otherwise chemostatic C-Q graph. These C-Q patterns reflect the relative control of two end-member sources of water contributing to the stream, dilute melt-driven surface runoff and higher-concentration groundwater. This result is similar to the multiple end-members noted by Zhi et al. (2019) that control the degree of chemostasis in simulations at the Coal Creek study watershed, based on the distinction of their chemistries. Without melt, the watershed reverts to a mostly single-member system dominated by groundwater, which produces much more constant concentrations over time.

Melt inputs also decrease concentrations of reactive ions in the stream due to overall dilution while increasing discharge throughout the year. The difference in discharge dominates the difference in concentration, leading to a higher export of reactive ions from the watershed with melt, consistent with a global study showing higher weathering yields in glacierized watersheds compared to non-

646 glacierized (Torres et al., 2017). This suggests that with the retreat of glaciers, export of reactive ions,
647 including nutrients, may decrease even if stream concentrations increase due to higher ET relative
648 to infiltration, which may have implications for downstream ecosystems. Actual changes, however,
649 will depend on other future changes in temperature, precipitation, and vegetative cover.

650 **Acknowledgments**

651 Funding from NSF (EAR-1759071) supported this work. Saberi also received financial support from
652 University of Minnesota. The authors would like to acknowledge Daniel Stanton and Andy Wickert
653 (University of Minnesota) for helpful discussions; Chloe Shaw and Emily Carlson (Gustavus Adol-
654 phus College) for fieldwork help; Carla Manciatì, Xavier Zapata, and Veronica Minaya (Escuela
655 Politecnica Nacional, Quito) for assistance in field site access; and Scott Alexander (University of
656 Minnesota) for lab support. The Flux-PIHM version 0.10.0 used for this paper is available on GitHub,
657 at <https://github.com/PSUmodeling/MM-PIHM/releases/tag/v0.10.0-alpha>. Field data collected and
658 used in this work is available at: [https://www.hydroshare.org/resource/d390906d0ed8440b9e3df8c48](https://www.hydroshare.org/resource/d390906d0ed8440b9e3df8c48075c454/)
659 [075c454/](https://www.hydroshare.org/resource/d390906d0ed8440b9e3df8c48075c454/)

660 **References**

- 661 Andermann, C., Longuevergne, L., Bonnet, S., Crave, A., Davy, P., & Gloaguen, R. (2012, 1). Impact
662 of transient groundwater storage on the discharge of Himalayan rivers. *Nature Geoscience*,
663 5(2), 127–132. doi: 10.1038/ngeo1356
- 664 Bao, C., Li, L., Shi, Y., & Duffy, C. (2017). Understanding watershed hydrogeochemistry: 1.
665 development of rt-flux-pihm. *Water Resources Research*, 53(3), 2328–2345.
- 666 Baraer, M., McKenzie, J., Mark, B. G., Gordon, R., Bury, J., Condom, T., ... Fortner, S. K. (2015, 5).
667 Contribution of groundwater to the outflow from ungauged glacierized catchments: a multi-
668 site study in the tropical Cordillera Blanca, Peru. *Hydrological Processes*, 29(11), 2561–2581.
669 doi: 10.1002/hyp.10386
- 670 Baraer, M., McKenzie, J. M., Mark, B. G., Bury, J., & Knox, S. (2009, 10). Characterizing
671 contributions of glacier melt and groundwater during the dry season in a poorly gauged
672 catchment of the Cordillera Blanca (Peru). *Advances in Geosciences*, 22, 41–49. doi:
673 10.5194/adgeo-22-41-2009
- 674 Barba, D., Robin, C., Samaniego, P., & Eissen, J.-P. (2008). Holocene recurrent explosive activity
675 at Chimborazo volcano (Ecuador). *Journal of Volcanology and Geothermal Research*, 176(1),
676 27–35.
- 677 Barba, D., Samaniego, P., Eissen, J.-P., Robin, C., Fornari, M., Cotten, J., & Beate, B. (2005).
678 Geology and structure of the late Pleistocene to Holocene Chimborazo stratovolcano (Ecuador
679). *6th International Symposium on Andean Geodynamics (ISAG 2005, Barcelona)*(January),
680 90–93.
- 681 Barnett, T. P., Adam, J. C., & Lettenmaier, D. P. (2005, 11). Potential impacts of a warming climate
682 on water availability in snow-dominated regions. *Nature*, 438(7066), 303–309. doi: 10.1038/
683 nature04141
- 684 Baronas, J. J., Torres, M. A., Clark, K. E., & West, A. J. (2017). Mixing as a driver of temporal
685 variations in river hydrochemistry: 2. major and trace element concentration dynamics in the
686 andes-amazon transition. *Water Resources Research*, 53(4), 3120–3145.
- 687 Bartoli, F., Poulencq, A., & Schouller, B. (2007). Influence of allophane and organic matter contents
688 on surface properties of andosols. *European journal of soil science*, 58(2), 450–464.
- 689 Benettin, P., Bailey, S. W., Campbell, J. L., Green, M. B., Rinaldo, A., Likens, G. E., ... Botter,
690 G. (2015). Linking water age and solute dynamics in streamflow at the Hubbard Brook
691 experimental forest, NH, USA. *Water Resources Research*, 51(11), 9256–9272.
- 692 Bhatt, G., Kumar, M., & Duffy, C. J. (2014, 12). A tightly coupled GIS and distributed hydrologic
693 modeling framework. *Environmental Modelling & Software*, 62, 70–84. doi: 10.1016/j.envsoft
694 .2014.08.003
- 695 Bradley, R. S. (2006, 6). CLIMATE CHANGE: Threats to Water Supplies in the Tropical Andes.
696 *Science*, 312(5781), 1755–1756. doi: 10.1126/science.1128087
- 697 Bradley, R. S., Vuille, M., Hardy, D., & Thompson, L. G. (2003, 2). Low latitude ice cores record
698 Pacific sea surface temperatures. *Geophysical Research Letters*, 30(4), 2–5. doi: 10.1029/
699 2002GL016546
- 700 Brantley, S. L., Kubicki, J. D., & White, A. F. (2008). Kinetics of water-rock interaction.
- 701 Brighenti, S., Tolotti, M., Bruno, M. C., Wharton, G., Pusch, M. T., & Bertoldi, W. (2019). Ecosys-
702 tem shifts in alpine streams under glacier retreat and rock glacier thaw: A review. *The Science
703 of the total environment*, 675, 542–559.
- 704 Brown, G. H. (2002). Glacier meltwater hydrochemistry. *Applied Geochemistry*, 17(7), 855–883.
- 705 Buytaert, W., & Beven, K. (2011, 5). Models as multiple working hypotheses: hydrological
706 simulation of tropical alpine wetlands. *Hydrological Processes*, 25(11), 1784–1799. doi:
707 10.1002/hyp.7936
- 708 Buytaert, W., Célleri, R., De Bièvre, B., Cisneros, F., Wyseure, G., Deckers, J., & Hofstede, R.
709 (2006, 11). Human impact on the hydrology of the Andean páramos. *Earth-Science Reviews*,
710 79(1-2), 53–72. doi: 10.1016/j.earscirev.2006.06.002
- 711 Clapperton, C. M. (1990, 1). Glacial and volcanic geomorphology of the Chimborazo-Carihuairazo
712 Massif, Ecuadorian Andes. *Transactions of the Royal Society of Edinburgh: Earth Sciences*,
713 81(02), 91–116. doi: 10.1017/S0263593300005174

- 714 Clow, D. W., & Mast, M. A. (2010). Mechanisms for chemostatic behavior in catchments: implica-
715 tions for co₂ consumption by mineral weathering. *Chemical Geology*, 269(1-2), 40–51.
- 716 Collins, D. N. (1999). Solute flux in meltwaters draining from a glacierized basin in the karakoram
717 mountains. *Hydrological processes*, 13(18), 3001–3015.
- 718 Devito, K., Creed, I., Gan, T., Mendoza, C., Petrone, R., Silins, U., & Smerdon, B. (2005). A
719 framework for broad-scale classification of hydrologic response units on the boreal plain: Is
720 topography the last thing to consider? *Hydrological Processes: An International Journal*,
721 19(8), 1705–1714.
- 722 Ek, M. B., Mitchell, K. E., Lin, Y., Rogers, E., Grunmann, P., Koren, V., ... Tarpley, J. D. (2003). Im-
723 plementation of Noah land surface model advances in the National Centers for Environmental
724 Prediction operational mesoscale Eta model. *Journal of Geophysical Research: Atmospheres*,
725 108(D22).
- 726 Engel, M., Penna, D., Bertoldi, G., Dell’Agnese, A., Soulsby, C., & Comiti, F. (2016, 1). Identifying
727 run-off contributions during melt-induced run-off events in a glacierized alpine catchment.
728 *Hydrological Processes*, 30(3), 343–364. doi: 10.1002/hyp.10577
- 729 Engel, M., Penna, D., Bertoldi, G., Vignoli, G., Tirlor, W., & Comiti, F. (2019). Controls on spatial
730 and temporal variability of streamflow and hydrochemistry in a glacierized catchment.
- 731 Farvolden, R. (1963). Geologic controls on ground-water storage and base flow. *Journal of hydrology*,
732 1(3), 219–249.
- 733 Favier, V. (2004). Glaciers of the outer and inner tropics: A different behaviour but a common
734 response to climatic forcing. *Geophysical Research Letters*, 31(16), L16403. doi: 10.1029/
735 2004GL020654
- 736 Feng, F., Li, Z., Jin, S., Dong, Z., & Wang, F. (2012). Hydrochemical characteristics and solute dy-
737 namics of meltwater runoff of urumqi glacier no. 1, eastern tianshan, northwest china. *Journal*
738 *of Mountain Science*, 9(4), 472–482.
- 739 Fortner, S. K., Mark, B. G., McKenzie, J. M., Bury, J., Trierweiler, A., Baraer, M., ... Munk, L.
740 (2011). Elevated stream trace and minor element concentrations in the foreland of receding
741 tropical glaciers. *Applied Geochemistry*, 26(11), 1792–1801.
- 742 Francou, B. (2004). New evidence for an ENSO impact on low-latitude glaciers: Antizana 15,
743 Andes of Ecuador. *Journal of Geophysical Research*, 109(D18), D18106. doi: 10.1029/
744 2003JD004484
- 745 Gibbs, R. (1967). The geochemistry of the amazon river system: Part 1. *The factors that control the*
746 *salinity and the composition and concentration of the suspended solids. Geological Society of*
747 *American Bulletin*, 78, 1203–1232.
- 748 Godsey, S. E., Kirchner, J. W., & Clow, D. W. (2009). Concentration–discharge relationships re-
749 flect chemostatic characteristics of us catchments. *Hydrological Processes: An International*
750 *Journal*, 23(13), 1844–1864.
- 751 Godsey, S. E., Kirchner, J. W., & Tague, C. L. (2014). Effects of changes in winter snowpacks
752 on summer low flows: Case studies in the Sierra Nevada, California, USA. *Hydrological*
753 *Processes*, 28(19), 5048–5064. doi: 10.1002/hyp.9943
- 754 Harrington, J. S., Mozil, A., Hayashi, M., & Bentley, L. R. (2018). Groundwater flow and storage
755 processes in an inactive rock glacier. *Hydrological Processes*, 32(20), 3070–3088.
- 756 Helgeson, H. C., Murphy, W. M., & Aagaard, P. (1984). Thermodynamic and kinetic constraints on
757 reaction rates among minerals and aqueous solutions. ii. rate constants, effective surface area,
758 and the hydrolysis of feldspar. *Geochimica et Cosmochimica Acta*, 48(12), 2405–2432.
- 759 Hem, J. D. (1985). *Study and interpretation of the chemical characteristics of natural water* (Vol.
760 2254). Department of the Interior, US Geological Survey.
- 761 Herndon, E. M., Dere, A. L., Sullivan, P., Norris, D., Reynolds, B., & Brantley, S. L. (2015). Land-
762 scape heterogeneity drives contrasting concentration–discharge relationships in shale headwa-
763 ter catchments.
- 764 Hindshaw, R. S., Tipper, E. T., Reynolds, B. C., Lemarchand, E., Wiederhold, J. G., Magnusson, J.,
765 ... Bourdon, B. (2011). Hydrological control of stream water chemistry in a glacial catchment
766 (damma glacier, switzerland). *Chemical Geology*, 285(1-4), 215–230.
- 767 Hood, J. L., Roy, J. W., & Hayashi, M. (2006). Importance of groundwater in the water balance
768 of an alpine headwater lake. *Geophysical Research Letters*, 33(13), 1–5. doi: 10.1029/

2006GL026611

- 769 Huth, A. K., Leydecker, A., Sickman, J. O., & Bales, R. C. (2004). A two-component hydrograph
770 separation for three high-elevation catchments in the Sierra Nevada, California. *Hydrological*
771 *Processes*, 18(9), 1721–1733. doi: 10.1002/hyp.1414
- 772 INEC. (2010). Censos de Poblacion y Vivienda 2010. *Quito, Ecuador*.
- 773 IPCC, C. C. (2007). Impacts, adaptation and vulnerability. contribution of working group ii to the
774 fourth assessment report of the intergovernmental panel on climate change. *Intergovernmental*
775 *Panel on Climate Change (IPCC)*, Cambridge University Press, New York.
- 776 Johnson, N. M., Likens, G. E., Bormann, F., Fisher, D., & Pierce, R. (1969). A working model for the
777 variation in stream water chemistry at the hubbard brook experimental forest, new hampshire.
778 *Water Resources Research*, 5(6), 1353–1363.
- 779 Kaser, G., Grosshauser, M., & Marzeion, B. (2010). Contribution potential of glaciers to water
780 availability in different climate regimes. *Proceedings of the National Academy of Sciences*,
781 107(47), 20223–20227. doi: 10.1073/pnas.1008162107
- 782 Kaser, G., & Osmaston, H. (2002). *Tropical glaciers*. Cambridge University Press.
- 783 Katsuyama, M., Tani, M., & Nishimoto, S. (2010). Connection between streamwater mean residence
784 time and bedrock groundwater recharge/discharge dynamics in weathered granite catchments.
785 *Hydrological Processes*, 24(16), 2287–2299.
- 786 Kumar, N., Ramanathan, A., Tranter, M., Sharma, P., Pandey, M., Ranjan, P., & Raju, N. J. (2019).
787 Switch in chemical weathering caused by the mass balance variability in a himalayan glacier-
788 ized basin: a case of chhota shigri glacier. *Hydrological sciences journal*, 64(2), 179–189.
- 789 La Frenierre, J., & Mark, B. G. (2014, 4). A review of methods for estimating the contribution
790 of glacial meltwater to total watershed discharge. *Progress in Physical Geography*, 38(2),
791 173–200. doi: 10.1177/0309133313516161
- 792 La Frenierre, J., & Mark, B. G. (2017). Detecting Patterns of Climate Change at Volcán Chimborazo,
793 Ecuador, by Integrating Instrumental Data, Public Observations, and Glacier Change Analysis.
794 *Annals of the American Association of Geographers*, 107(4), 979–997. doi: 10.1080/24694452
795 .2016.1270185
- 796 Lasaga, A. C. (1984). Chemical kinetics of water-rock interactions. *Journal of geophysical research:*
797 *solid earth*, 89(B6), 4009–4025.
- 798 Lewis, T., Lafrenière, M. J., & Lamoureux, S. F. (2012). Hydrochemical and sedimentary responses
799 of paired high arctic watersheds to unusual climate and permafrost disturbance, cape bounty,
800 melville island, canada. *Hydrological Processes*, 26(13), 2003–2018.
- 801 Li, L., Bao, C., Sullivan, P. L., Brantley, S., Shi, Y., & Duffy, C. (2017). Understanding wa-
802 tershed hydrogeochemistry: 2. synchronized hydrological and geochemical processes drive
803 stream chemostatic behavior. *Water Resources Research*, 53(3), 2346–2367.
- 804 Maher, K. (2011). The role of fluid residence time and topographic scales in determining chemical
805 fluxes from landscapes. *Earth and Planetary Science Letters*, 312(1-2), 48–58.
- 806 Mark, B. G., French, A., Baraer, M., Carey, M., Bury, J., Young, K. R., ... Lutz, L. (2017).
807 Glacier loss and hydro-social risks in the Peruvian Andes. *Global and Planetary Change*,
808 159(October), 61–76. doi: 10.1016/j.gloplacha.2017.10.003
- 809 Mark, B. G., & Mckenzie, J. M. (2007, 10). Tracing Increasing Tropical Andean Glacier Melt with
810 Stable Isotopes in Water. *Environmental Science & Technology*, 41(20), 6955–6960. doi:
811 10.1021/es071099d
- 812 Mayer, K. U., Frind, E. O., & Blowes, D. W. (2002). Multicomponent reactive transport modeling
813 in variably saturated porous media using a generalized formulation for kinetically controlled
814 reactions. *Water Resources Research*, 38(9), 13–1.
- 815 McClain, M. E., & Naiman, R. J. (2008). Andean influences on the biogeochemistry and ecology of
816 the amazon river. *BioScience*, 58(4), 325–338.
- 817 McGuire, K., McDonnell, J. J., Weiler, M., Kendall, C., McGlynn, B., Welker, J., & Seibert, J.
818 (2005). The role of topography on catchment-scale water residence time. *Water Resources*
819 *Research*, 41(5).
- 820 McLaughlin, R. (2017). *Hydrochemical Signatures of Glacial Meltwater on Volcán Chimborazo,*
821 *Ecuador* (Unpublished doctoral dissertation).

- 823 Messerli, B., Viviroli, D., & Weingartner, R. (2004). Mountains of the World: Vulnerable Water
824 Towers for the 21st Century. *Ambio*, 29–34.
- 825 Milner, A. M., Brown, L. E., & Hannah, D. M. (2009). Hydroecological response of river systems
826 to shrinking glaciers. *Hydrological Processes: An International Journal*, 23(1), 62–77.
- 827 Milner, A. M., Khamis, K., Battin, T. J., Brittain, J. E., Barrand, N. E., Füreder, L., ... others (2017).
828 Glacier shrinkage driving global changes in downstream systems. *Proceedings of the National
829 Academy of Sciences*, 114(37), 9770–9778.
- 830 Minaya, V. G., Maldonado. (2016). Ecohydrology of the Andes Páramo Region. *PhD diss., IHE
831 Delft Institute for Water Education*.
- 832 Moriasi, D. N., Arnold, J. G., Van Liew, M. W., Bingner, R. L., Harmel, R. D., & Veith, T. L.
833 (2007). Model evaluation guidelines for systematic quantification of accuracy in watershed
834 simulations. *Transactions of the ASABE*, 50(3), 885–900.
- 835 Nash, J., & Sutcliffe, J. (1970). River forecasting using conceptual models: Part 1—a discussion of
836 principles. *Journal of Hydrology*, 10(3), 280–290.
- 837 Ostheimer, G. J., Hadjivasiliou, H., Kloer, D. P., Barkan, A., & Matthews, B. W. (2005). Struc-
838 tural analysis of the group ii intron splicing factor crs2 yields insights into its protein and rna
839 interaction surfaces. *Journal of molecular biology*, 345(1), 51–68.
- 840 Pepin, N., Bradley, R. S., Diaz, H. F., Baraer, M., Caceres, E. B., Forsythe, N., ... Yang, D. Q. (2015,
841 5). Elevation-dependent warming in mountain regions of the world. *Nature Climate Change*,
842 5(5), 424–430. doi: 10.1038/nclimate2563
- 843 Podwojewski, P., Poulenard, J., Zambrana, T., & Hofstede, R. (2002). Overgrazing effects on vege-
844 tation cover and properties of volcanic ash soil in the páramo of Llangahua and al Esperanza
845 (Tungurahua, Ecuador). *Management*, 18, 45–55. doi: 10.1079/SUM2001100
- 846 Pohl, E., Knoche, M., Gloaguen, R., Andermann, C., & Krause, P. (2015, 7). Sensitivity analysis
847 and implications for surface processes from a hydrological modelling approach in the Gunt
848 catchment, high Pamir Mountains. *Earth Surface Dynamics*, 3(3), 333–362. doi: 10.5194/
849 esurf-3-333-2015
- 850 Poppe, L., Paskevich, V., Hathaway, J., & Blackwood, D. (2001). A laboratory manual for x-ray
851 powder diffraction. *US Geological Survey open-file report*, 1(041), 1–88.
- 852 Qu, Y., & Duffy, C. J. (2007, 8). A semidiscrete finite volume formulation for multiprocess watershed
853 simulation. *Water Resources Research*, 43(8), 1–18. doi: 10.1029/2006WR005752
- 854 Saberi, L., McLaughlin, R. T., Crystal Ng, G., La Frenierre, J., Wickert, A. D., Baraer, M., ...
855 Mark, B. G. (2019). Multi-scale temporal variability in meltwater contributions in a tropical
856 glacierized watershed. *Hydrology and Earth System Sciences*, 23(1), 405–425.
- 857 Samaniego, P., Barba, D., Robin, C., Fornari, M., & Bernard, B. (2012, 4). Eruptive history of
858 Chimborazo volcano (Ecuador): A large, ice-capped and hazardous compound volcano in the
859 Northern Andes. *Journal of Volcanology and Geothermal Research*, 221–222, 33–51. doi:
860 10.1016/j.jvolgeores.2012.01.014
- 861 Shanley, J. B., McDowell, W. H., & Stallard, R. F. (2011). Long-term patterns and short-term
862 dynamics of stream solutes and suspended sediment in a rapidly weathering tropical watershed.
863 *Water Resources Research*, 47(7).
- 864 Shi, Y., Davis, K. J., Duffy, C. J., & Yu, X. (2013, 10). Development of a Coupled Land Surface Hy-
865 drologic Model and Evaluation at a Critical Zone Observatory. *Journal of Hydrometeorology*,
866 14(5), 1401–1420. doi: 10.1175/JHM-D-12-0145.1
- 867 Shoji, S., Nanzyo, M., & Dahlgren, R. (1994). *Volcanic ash soils: genesis, properties and utilization*.
868 Elsevier.
- 869 Sicart, J. E., Hock, R., & Six, D. (2008, 12). Glacier melt, air temperature, and energy balance in
870 different climates: The Bolivian Tropics, the French Alps, and northern Sweden. *Journal of
871 Geophysical Research*, 113(D24), D24113. doi: 10.1029/2008JD010406
- 872 Smith, J. A., Mark, B. G., & Rodbell, D. T. (2008). The timing and magnitude of mountain glaciation
873 in the tropical andes. *Journal of Quaternary Science: Published for the Quaternary Research
874 Association*, 23(6–7), 609–634.
- 875 Somers, L. D., McKenzie, J. M., Mark, B. G., Lagos, P., Ng, G.-H. C., Wickert, A. D., ... Silva, Y.
876 (2019). Groundwater buffers decreasing glacier melt in an andean watershedbut not forever.
877 *Geophysical Research Letters*, 46(22), 13016–13026.

- 878 Stachnik, Ł., Majchrowska, E., Yde, J. C., Nawrot, A. P., Cichała-Kamrowska, K., Ignatiuk, D., &
879 Piechota, A. (2016). Chemical denudation and the role of sulfide oxidation at werenskiold-
880 breen, svalbard. *Journal of Hydrology*, *538*, 177–193.
- 881 Stallard, & Edmond. (1983). Geochemistry of the amazon: 2. the influence of geology and weather-
882 ing environment on the dissolved load. *Journal of Geophysical Research: Oceans*, *88*(C14),
883 9671–9688.
- 884 Stallard, R. F., & Murphy, S. F. (2014). A unified assessment of hydrologic and biogeochemical
885 responses in research watersheds in eastern puerto rico using runoff–concentration relations.
886 *Aquatic geochemistry*, *20*(2-3), 115–139.
- 887 Stern, C. R. (2004). Active andean volcanism: its geologic and tectonic setting. *Revista geológica*
888 *de Chile*, *31*(2), 161–206.
- 889 Tague, C., Grant, G., Farrell, M., Choate, J., & Jefferson, A. (2008, 1). Deep groundwater mediates
890 streamflow response to climate warming in the Oregon Cascades. *Climatic Change*, *86*(1-2),
891 189–210. doi: 10.1007/s10584-007-9294-8
- 892 Takahashi, T., & Shoji, S. (2002). Distribution and classification of volcanic ash soils. *GLOBAL*
893 *ENVIRONMENTAL RESEARCH-ENGLISH EDITION-*, *6*(2), 83–98.
- 894 Tetzlaff, D., Seibert, J., McGuire, K., Laudon, H., Burns, D. A., Dunn, S., & Soulsby, C. (2009).
895 How does landscape structure influence catchment transit time across different geomorphic
896 provinces? *Hydrological Processes: An International Journal*, *23*(6), 945–953.
- 897 Torres, M. A., Moosdorf, N., Hartmann, J., Adkins, J. F., & West, A. J. (2017). Glacial weathering,
898 sulfide oxidation, and global carbon cycle feedbacks. *Proceedings of the National Academy of*
899 *Sciences*, *114*(33), 8716–8721.
- 900 Torres, M. A., West, A. J., & Clark, K. E. (2015). Geomorphic regime modulates hydrologic control
901 of chemical weathering in the andes–amazon. *Geochimica et Cosmochimica Acta*, *166*, 105–
902 128.
- 903 Tranter, M., Brown, G. H., Hodson, A. J., & Gurnell, A. M. (1996). Hydrochemistry as an indicator
904 of subglacial drainage system structure: a comparison of alpine and sub-polar environments.
905 *Hydrological Processes*, *10*(4), 541–556.
- 906 Ugolini, F. C., Dahlgren, R. A., et al. (2002). Soil development in volcanic ash. *GLOBAL ENVI-*
907 *RONMENTAL RESEARCH-ENGLISH EDITION-*, *6*(2), 69–82.
- 908 Veettil, B. K., Leandro Bayer Maier, E., Bremer, U. F., & de Souza, S. F. (2014, 12). Combined
909 influence of PDO and ENSO on northern Andean glaciers: a case study on the Cotopaxi ice-
910 covered volcano, Ecuador. *Climate Dynamics*, *43*(12), 3439–3448. doi: 10.1007/s00382-014
911 -2114-8
- 912 Vermote, E. (2015). MOD09A1 MODIS/Terra Surface Reflectance 8-Day L3 Global 500m SIN
913 Grid V006. *NASA EOSDIS Land Processes DAAC*.
- 914 Vuille, M., & Bradley, R. S. (2000). the tropical Andes. *Geophysical Research Letters*, *27*(23),
915 3885–3888.
- 916 Vuille, M., Francou, B., Wagnon, P., Juen, I., Kaser, G., Mark, B. G., & Bradley, R. S. (2008, 8).
917 Climate change and tropical Andean glaciers: Past, present and future. *Earth-Science Reviews*,
918 *89*(3-4), 79–96. doi: 10.1016/j.earscirev.2008.04.002
- 919 Vuille, M., & Keimig, F. (2004, 9). Interannual Variability of Summertime Convective Cloudiness
920 and Precipitation in the Central Andes Derived from ISCCP-B3 Data. *Journal of Climate*,
921 *17*(17), 3334–3348. doi: 10.1175/1520-0442(2004)017<3334:IVOSCC>2.0.CO;2
- 922 Wagnon, P., Ribstein, P., Francou, B., & Sicart, J. E. (2001). Anomalous heat and mass budget of
923 Glaciar Zongo , Bolivia , during the 1997 / 98 El Ni · o year. *Journal of Glaciology*, *47*(156),
924 21–28.
- 925 Wen, H., Perdrial, J., Bernal, S., Abbott, B. W., Dupas, R., Godsey, S. E., ... others (2020). Tem-
926 perature controls production but hydrology controls export of dissolved organic carbon at the
927 catchment scale.
- 928 White, A. F., Blum, A. E., Schulz, M. S., Vivit, D. V., Stonestrom, D. A., Larsen, M., ... Eberl,
929 D. (1998). Chemical weathering in a tropical watershed, luquillo mountains, puerto rico:
930 I. long-term versus short-term weathering fluxes. *Geochimica et Cosmochimica Acta*, *62*(2),
931 209–226.
- 932 Williams, M. W., Hood, E., Molotch, N. P., Caine, N., Cowie, R., & Liu, F. (2015). The teflon

- 933 basinmyth: hydrology and hydrochemistry of a seasonally snow-covered catchment. *Plant*
934 *Ecology & Diversity*, 8(5-6), 639–661.
- 935 Wilson, A. M., Williams, M. W., Kayastha, R. B., & Racoviteanu, A. (2016, 3). Use of a hydrologic
936 mixing model to examine the roles of meltwater, precipitation and groundwater in the Langtang
937 River basin, Nepal. *Annals of Glaciology*, 57(71), 155–168. doi: 10.3189/2016AoG71A067
- 938 Wolery, T. J. (1992). Eq3/6, a software package for geochemical modeling of aqueous systems:
939 package overview and installation guide (version 7.0).
- 940 Zhi, W., Li, L., Dong, W., Brown, W., Kaye, J., Steefel, C., & Williams, K. H. (2019). Distinct
941 source water chemistry shapes contrasting concentration-discharge patterns. *Water Resources*
942 *Research*, 55(5), 4233–4251.